SURFACE INTERACTION, POLARIZATION AND MOLECULAR WEIGHT EFFECTS FOR A WHISPERING GALLERY MODE SENSOR

DISSERTATION

Submitted in Partial Fulfillment

of the Requirements for the

Degree of

DOCTOR OF PHILOSOPHY (Materials Chemistry)

at the

POLYTECHNIC UNIVERSITY

by

Mayumi Noto

May 2005

Approved:

_____
Department Head

_____20____

Copy No._____

Approved by the Guidance Committee:

Major: Materials Chemistry

_____

Stephen Arnold
University Professor of Physics, Polytechnic University

Minor: Polymer Chemistry

_____

Iwao Teraoka
Associate Professor of Chemistry, Polytechnic University

Committee Member:

_____

Bruce Garetz
Professor of Chemistry, Polytechnic University

Committee Member:

_____

Kalle Levon
Professor and Vice Provost for Research
Polymer Research Institute, Polytechnic University

VITA

Mayumi Noto was born on September 26, 1972 in Tokyo, Japan. She obtained a B.A. in Chemistry with honor from Hunter College of the City University of New York in 1998. After the graduation, she joined the cellulose fiber division of a British chemical company, Courtaulds plc, in Tokyo. Two years of fiber technical marketing led her to pursue her interests in polymer chemistry. She started her graduate career at Polytechnic University in Brooklyn, NY in September 2000. She completed her Master's degree under the guidance of Professor Richard Gross in June 2002, in which she learned enzyme immobilization methods and their applications for polyester syntheses. She joined Microparticle Photophysics Lab (MP^3L) in July 2002 to develop a new biosensor based on a frequency shift of a Whispering Gallery mode in silica microsphere. Under the guidance of Professor Stephen Arnold, she focused her effort in extending the WGM sensor applications from protein detection to layer thickness measurements and the determination of a molecular orientation on the silica surface. The contents of this dissertation work have been published and will be submitted for publication in peer-reviewed journals and as book chapters:

- M. Noto, F. Vollmer, D. Keng, I. Teraoka, and S. Arnold
  "Nanolayer characterization through wavelength multiplexing a microsphere resonator" Opt. Lett., 30, 510-512 (2005).

- S. Arnold, M. Noto, and F. Vollmer
  Consequences of extreme photon confinements in microcavities: I. Ultra-sensitive detection of perturbations by biomolecules in *Frontiers of optical spectroscopy: investigating extreme physical condition with advanced optical techniques*, Ed. by B. Di Bartolo (Kluwer Academic Publishers, Dordorecht, 2005), pp. 337-357.

In preparation

- M. Noto, M. Khoshsima, D. Keng, I. Teraoka, and S. Arnold
  "Molecular weight sensitivity of a whispering gallery mode sensor."
- M. Noto, O. Gaathon, D. Keng, I. Teraoka, and S. Arnold
  "Polarization effects on resonance frequency shifts of whispering gallery modes."

The research at MP^3L was supported by a grant from National Science Foundation.

Dedication

To my mother

Mitsuko Noto,

To my sister

Mina Noto

who sleeps in Enzan, Japan overlooking the beautiful vineyards.

Acknowledgement

I would like to thank my advisor, Dr. Stephen Arnold. Steve has been a great mentor and the source of inspiration. He showed me the beauty and the excitement of interdisciplinary science. I was fortunate to be one of his students and learn his rigorous scientific approach in theory and experiment. Steve, I promise I will get a good pair of gloves and boots when I get my own motorcycle license.

I would like to thank my committee members, Professor Iwao Teraoka, Professor Bruce Garetz, and Professor Kalle Levon for their guidance. Professor Teraoka's detailed electromagnetic calculations on WGM perturbations have led my experiments, and I appreciate the time he spent with me for the countless discussions. His sincere attitude towards science extends to his care for students. Professor Teraoka, *Hontouni*, *osewani narimashita. Arigatou gozaimsu*.

To Professor Neil Wotherspoon, David, Ophir, and Mumchil: without your support and collaboration on the projects, I would not have completed this thesis. Thank you. Neil, please take care. David, Ophir, and Mumchil, I wish you successful undergraduate and graduate career. I would also like to thank the past members of MP^3L, Mazi, Jason and Steve of Novawave Technologies for valuable discussions.

To all my friends at Polytechnic University, we shared laughs and tears. I cherish your friendships and wish you all the best.

Anita and Stephanie, since the day we met at Hunter College, you have been there for me. You guys are the best. Thank you.

Above all, I would like to thank Frank Vollmer, my collaborator and partner. I am grateful for your support and love. I respect and admire your scientific vigor and creativity.

Finally, I would like to thank New York City. It is the best city in the world.

Abstract

SURFACE INTERACTION, POLARIZATION AND MOLECULAR WEIGHT EFFECTS FOR A WHISPERING GALLERY MODE SENSOR

Mayumi Noto

In this thesis, we investigate the use of an optical resonance of a microsphere in measuring the thickness and dielectric constant of a bio-nano-layer and in determining the molecular orientation of an adsorbate at the sphere surface. We also establish the molecular weight sensitivity of the resonance frequency shift.

The resonances of silica microspheres can be very narrow (i.e. high Quality Factor, Q) and as a result are extremely sensitive to dielectric perturbations at the sphere surface. In particular, one may use the shift of the resonant frequency to detect the adsorption of bio-molecules with unprecedented sensitivity.

This work goes beyond the detection of nanoscopic bio-molecules to the characterization of polymer layers ~100 nm in thickness. The possibility of enlarging the scope of the sensor is inspired by first order perturbation theory. The theory reveals that the evanescent field decay length influences resonance shifts and may be used as a nanoscopic ruler. Through this theoretical discussion, the idea of using the two light sources to stimulate resonances in an individual microsphere precipitated. Microsphere Wavelength Multiplexing (MWM) experiments proved the theory to be sound. The measurement of simultaneous shifts of two resonances at widely separated wavelengths allowed us to determine the thickness and the dielectric excess of an important bio-nanolayer (poly-L-lysine) even though its refractive index only exceeded that of the aqueous buffer solution by 0.0012.

We revisited protein adsorption and investigated the molecular weight MW sensitivity of the sensor. We found that the resonance shift is proportional to $MW^{1/3}$. A new theoretical model explains the $MW^{1/3}$ dependence and concludes that spherical protein covers 34% of the microsphere surface and the effective layer refractive index is 1.39.

We demonstrate polarization specific stimulation of resonances and measure TE and TM mode shifts by inducing a refractive index change in the medium. NaCl addition experiment confirms TM to TE shift ratio predicted by perturbation theory. The polarization specific measurement is applied to investigate the orientation of phenol molecule at the silica surface.

Table of Contents:

Chapter **Page**

Chapter 1

Introduction 19

Chapter 2

The WGM Sensor 21

2.1 Optical Resonances and Silica Microspheres 21

2.2 High Q Resonances and Sensitive Detection 22

2.3 Theoretical Approach: Quantum Analog 25

2.4 First Order Perturbation Theory 28

Chapter 3

The WGM Sensor Setup 30

3.1 Distributed Feedback Laser 30

3.2 Optical Circuit

3.2.1 1300 nm DFB Laser 31

3.2.2 760 nm DFB Laser 32

3.3 Optical Fiber 33

3.4 Sample Cell 33

3.5 Detector 34

3.6 Data Acquisition 34

3.7 Microsphere 35

Chapter 4

Study of Nanolayer Adsorption:

Layer Characterization by Wavelength Multiplexing of Microsphere 36

4.1 Soft Condensed Bio-Layers 36

4.2 The Evanescent Field 36

4.3 The Evanescent Field Length 37

4.4 The General Form of First Order Perturbation Theory 39

4.5 Two-Wavelength Measurements 40
4.6 Experimental Approach 42
4.7 Verification of Two Limiting Cases 44
4.7.1 BSA Adsorption Experiment 44
4.7.2 NaCl Experiment 46
4.7.3 Theory and Experiment 47
4.8 Poly-L-Lysine Measurements 48
4.9 Conclusion 50
Chapter 5
Molecular Weight Dependence of the WGM Sensor 52
5.1 Thin Protein Layer Analyses 52
5.2 Protein Interaction at Solid Surfaces 52
5.3 Factors Controlling Protein Adsorption 54
5.4 Silica Surface and Modification Methods 54
5.5 Molecular Weight Dependence Experiments 57
5.5.1 Protein Sample Preparation 57
5.5.2 Adsorption Experiments 58
5.6 Data Interpretations 63
5.7 Refractive index change in the medium due to the addition of protein 65
5.8 Conclusion 66
Chapter 6
Polarization Dependence of Resonance Shifts 67
6.1 Two Polarizations of Microsphere Resonances 67
6.2 TE and TM Shift Differences 69
6.3 Polarization-Specific WGM Stimulation 73
6.4 NaCl Experiments 75
6.5 α-Lactalbumin Experiments 77
6.6 Ethylene Glycol Experiments 79
6.7 Phenol Molecules at Surface 81
6.8 TE and TM Shift and Molecular Orientation 84

6.9 Conclusion 87

Chapter 7

The Future Generation of a Whispering gallery Mode Sensor 89

References 90

Appendix 1

Laplace Transform 96

Appendix 2

Surface Modification Methods 98

Appendix 3

Resonance Mode Number ℓ 101

Appendix 4

Uniform Refractive Index Change in the Surrounding Medium and the Resonance Shift 102

Appendix 5

Publication 103

Symbols Used

Symbol	Description	Page
WGM	Whispering Gallery Mode	19
QCM	Quartz Crystal Microbalance	19
SPR	Surface Plasmon Resonance	19
ATR-FTIR	Attenuated Total Reflectance and Fourier Transform Infrared	19
TE	Transverse Electric	20
TM	Transverse Magnetic	20
Q	Quality factor	21
ω	Angular frequency	22
τ	Photon lifetime (s^{-1})	22
γ	Decay rate	22
t	Layer thickness	24
R	Microsphere radius	24
λ	Wavelength	24
μ	Reduced mass	25
q	Particle charge	25
$\hbar$	(Plank's constant)/2π	25
ψ	Wave function	25
$\hat{L}$	Angular momentum operator	25
ℓ	Angular momentum quantum number	25
m	Azimuthal quantum number	25
$Y_{\ell,m}$	Spherical harmonic function	25
V_{eff}	Effective potential	26
E	Electric field	26
k	Propagation constant	26
c	Speed of light	26
n	Refractive index	26
k_0	Propagation constant in free space	27
$j_\ell(n_s k_0 r)$	Spherical Bessel function	27

Symbol	Description	Page
ε_{rs}	Relative permittivity of microsphere	29
ε_{rm}	Relative permittivity of medium	29
DFB	Distributed feedback laser	31
SMF	Single mode fiber	31
i	Laser drive current	31
HF	Hydrofluoric acid	33
PLL	Poly-L-lysine	36
p	Dipole moment	36
α_{ex}	Excess polarizability	36
L_c	Wavelength dependent evanescent field length	38
κ_e	Dielectric profile	39
S	Ratio of fractional wavelength shifts	41
BSA	Bovine serum albumin	44
PBS	Phosphate buffered saline	44
pI	Isoelectric point	44
R_a (R_d)	Rate of adsorption (desorption)	52
k_a (k_d)	Rate constant for association (dissociation)	52
θ	Fractional coverage	52
N	Number of surface binding site	52
K_e	Equilibrium constant	53
E_a	Activation energy	53
R_{gas}	Gas constant	53
T	Temperature	53
Γ_{SiOH}	Surface density of SiOH	55
MW	Molecule weight	57
LA	α-Lactalbumin	63
N_A	Avogadro's number	64
ρ_p	protein mass density	64
f	Volume fraction	64
A_p	Area occupied by a protein molecule	64

Symbol	Description	Page
dn/dc	Differential refractive index	65
ξ	Aspect ratio	65
ν	Mode order	67
α_ν	Root of the Airy function	67
D	Electric displacement	69
P	Induced dipole moment per unit volume	69
θ	Analyzer angle	73
ξ	Laser angle	73
EG	Ethylene glycol	79
ε_0	Permittivity constant	81
φ	Phenyl ring tilt angle	82
χ	Phenyl ring twist angle	82
α_{xx}, α_{yy}, α_{zz}	Polarizability tensor element	84
η	Phenyl ring azimuthal angle	85
a	A dielectric particle or protein radius	87
X(m)	Laplace transform	94
x(n)	Inverse Laplace transform	95
DMF	N,N-dimethylformamide	97
p	Momentum	99

Figures and Graphs

Figure	Description	Page
2A	Whispering Gallery Mode; 30 waves wraps around the circumference of the microsphere.	21
2B	Time domain plot of two oscillators with τ = 10 s (bold) and τ =100 s (thin). γ is the rate at which the energy decays (i.e. $\gamma = 1/\tau$).	22
2C	Frequency domain plot of two oscillators with $\gamma = 0.1\ s^{-1}$ (thin) and $\gamma = 0.01\ s^{-1}$ (bold).	23
2D	Schematic representation of frequency shifts with two linewidths: $\gamma = 0.01\ s^{-1}$ (right) and $0.1\ s^{-1}$ (left).	23
2E	Change in wavelength due to the microsphere radius increase.	24
2F	Effective potential of a hydrogen atom (thick line).	26
2G	The effective potential vs. (r/R) for a photonic atom. The sum of $\ell(\ell+1)/r^2$ and $(1-n^2)k_0^2$ terms is shown as the thick line. A pocket formed is the potential well.	28
3A	The basic WGM biosensor set up. A portion of the sample cell is magnified (and rotated by 180º about the z-axis to show the microsphere-fiber coupling).	30
3B	A simplex cord with a FC/PC connector. The FC/PC end is connected to the pigtailed laser and the bare fiber end is connected to the detector. Not to scale.	32
3C	The optical set up for the 760 nm DFB laser. The collimator lens and the isolator are housed inside a Teflon piece (1" diameter and 1/2" thick). The 780 HP bare fiber is passed through the cuvette and secured by epoxy as described in Chapter 3.4.	32
3D	Transmission spectrum recorded using 760 nm laser. The scan range is 0.04 nm (8mA). The width of a Lorenzian-shaped dip is 0.12 pm and Q is 6×10^6. Resonance coupling is about ~20% efficiency.	34
3E	Optical image of a fabricated silica microsphere. R_e = 204 μm.	35

Figure	Description	Page
4A	The evanescent field intensity profile from the sphere surface to radial distance r. The surface evanescent intensity is taken as 1.	39
4B	S, the ratio of $(\Delta\lambda/\lambda)_{760}$ and $(\Delta\lambda/\lambda)_{1310}$, against layer thickness t.	42
4C	Experimental set up for wavelength multiplexing of a microsphere.	42
4D	Transmission spectrum of the 760 nm laser (left) and the superposition of resonances from the two lasers (right).	43
4E	Resonance shift due to BSA adsorption: Resonance dip from the 760 nm laser (thin) and a dip from the 1310 nm laser (bold).	45
4F	Time trace of resonance positions, NaCl experiment: 760 nm (thin) and 1310 nm (bold).	46
4G	The plot of $(\Delta\lambda/\lambda)_{760}$ against $(\Delta\lambda/\lambda)_{1310}$. The points represent the actual data; the lines are from the perturbation theory.	47
4H	Structure of PLL. In water ~pH 7, amine and carboxyl groups are predominantly ionized.	48
4I	Resonance shifts due to PLL adsorption onto the silica microsphere. 100-point data smoothing applied.	49
4J	Illustration of a possible PLL chain arrangement near the surface. ■ is the positive charge on the polymer chain. ● is the surface negative charge. ○ and □ are ions in the solution.	50
5A	Energy diagram of analyte A and ligand L in the bound state (right) and unbound state (left). $E_{a,a}$ is the activation energy for association, and $E_{a,d}$ is for dissociation.	53
5B	Schematic representation of surface SiOH groups. The gray portion represents the bulk silica structure. Q^3: Single silanol, Q^2: Geminal, and Q^1: Silanetriol.	55
5C	Top: Typical silane coupling agents: tri-functional (left) and mono-functional (right). Bottom: General reaction scheme for 3-aminopropyltrimethoxysialne and silica surface.	56
5D	Cross-linking between adjacent silane coupling agents.	56

Figure	Description	Page
5E	Transmitted light intensity as a function of the laser current recorded in a γ-globulin experiment; A: the spectrum right before the protein injection, B: the spectrum at the end of the experiment. The positive ramp is due to the higher laser power output for the larger current input.	59
5F	Resonance dip position vs. time. γ-Globulin adsorption onto carboxylated microsphere surface at 0.93μM (thick line) and 0.18 μM (dotted line) concentrations.	60
5G	Adsorption isotherm of α-lactalbumin ( ), BSA ( ), and thyroglobulin ( ). The dotted lines are to guide your eyes.	61
5H	Resonance wavelength shifts against protein molecular weight in a double logarithmic scale. The data are the average of three measurements. The line was drawn manually to fit the data.	62
5I	The measured shifts against $MW^{1/3}$. Error bars show the spread of data from three measurements.	63
6A	Field orientations of TE and TM modes.	67
6B	Electric field at the boundary. Gray blocks indicate the dielectric materials such as silica. E is the electric field and D is the electric displacement.	69
6C	A dielectric particle in the static electric field E_0.	71
6D	TM to TE ratio of resonance shifts due to a single particle adsorption and a packed sphere layer formation (ℓ = 500 and n_s = 1.47 and n_m = 1.33). ν is a mode order. The figure was adopted from Ref. 57.	71
6E	TM to TE ratio for adsorption of a standing cylinder (line), a lying cylinder (dashed), a sphere (dotted), and a packed layer of spheres (dash-dotted). ν = 1, ℓ = 500 and n_s = 1.47 and n_m = 1.33 are used for the calculation. The figure was adopted from Ref. 57.	72
6F	The laser on a rotation stage and the analyzer placed in front of the detector to check the orientation of the light within the optical fiber. The sample cell is omitted for clarity.	73

Figure	Description	Page
6G	Rotation angle θ of the analyzer, plotted as a function of the rotation angle ξ of the laser.	74
6H	The laser rotation setup with a microsphere. The analyzer is used to check the polarization direction, but taken out for shift measurements and spectrum recordings. Note that the microsphere contacts the etched fiber at the sphere's equator (i.e., the largest radius) to ensure that the light orbit is in the equatorial plane.	74
6I	Resonance spectra at ξ = 0º (line) and 90º (dotted).	75
6J	The fractional resonance shifts due to NaCl addition: Measurements (symbols) and TM theory (line).	77
6K	The fractional resonance shifts due to NaCl addition: Measurements (symbols) and TE theory (line).	77
6L	Ethylene glycol structure, stick and ball model.	79
6M	Normalized fractional wavelength shifts against EG concentration. The expected shift from dn/dc is shown as a solid line (TM) and a dashed line (TE). The error bars indicate the spread of data for all prominent dips observed in two experiments.	80
6N	Phenol molecule. Z-axis points out of the xy plane.	82
6O	Expected phenol molecular orientation on silica surface. φ is the tilt angle and χ is the twist angle defined by the O-phenyl ring plane and the silica surface plane. When χ = 0º, the phenol molecular x-axis is parallel to the surface. The thick line indicates a hydrogen bonding between silanol and phenol.	82
6P	Normalized fractional wavelength shift due to phenol addition. The average of three experiments is plotted for TM ( ) and TE ( ). Calculated dn/dc shifts based on Eqn. 6.3 and 6.4 are shown as a solid line (TM) and a dotted line (TE).	83

Figure	Description	Page
6Q	Three angles to define phenol orientation in the laboratory frame XYZ. Tilt angle φ, twist angle χ, and the azimuthal angle η. The phenol oxygen is placed at the origin. The unit vectors $\mathbf{e_1}$, $\mathbf{e_2}$, and $\mathbf{e_3}$ are introduced as a frame fixed on the phenol molecular axis. The molecular y-axis is in the direction of $\mathbf{e_2}$. $\mathbf{e_1}$ and $\mathbf{e_3}$ rotate together around $\mathbf{e_2}$.	85
6R	α_{ZZ} and α_{XX} with respect to φ and χ angles (in radians).	86
1	Normalized κ_e profile for a layer. r =0 set at the sphere surface.	94
2	An example of a normalized κ_e, the function is $x(n) = e^{-n}$.	95
3	Photon circumnavigating the circumference of a microsphere.	99
Tables		
1	Refractive indices of water and silica.	41
2	Molecular weight and isoelectric point of five proteins.	57
3	Resonance positions for a sphere of R= 200 μm and n_s=1.47 in air (excitation wavelength λ_0 =1.3μm).	68
4	TM mode resonance shifts due to LA layer formation.	79
5	TE mode resonance shifts due to LA layer formation.	79

Chapter 1
Introduction

Dielectric microcavities confine photons to small volumes by total internal reflection and have size-dependent resonant frequency spectra. An ideal cavity would confine light for a long time (i.e., a time much greater than the diameter/light speed). Devices based on optical cavities can be found in a wide range of applications and studies such as semiconductor lasers and dynamic filters in optical communications.[1] Exciting new techniques are emerging from this field for biochemical and biomedical applications.

Here at Polytechnic University, I found a group of physicists, chemists, and electrical engineers, a truly interdisciplinary ensemble, with an interest in developing a new sensor based on optical microcavities. They managed to foster collaboration with biochemists at Rockefeller University, and succeeded in the first stage of developing a new sensing technique. This new emerging technique is called a Whispering Gallery Mode Sensor (WGM sensor). The WGM sensor has been demonstrated for protein detection and DNA single nucleotide mismatch.[2,3] The sensor is predicted to be capable of unlabelled single molecule detection.[4]

As a chemist, I was interested in studying protein-surface interactions and investigating the surface morphology of protein. When protein molecules form a layer on a surface, do these molecules have the same conformation? Once on the surface, do they reorient themselves to establish a denser and more stable layer?

Protein molecules are nanometers in size. If one wishes to study a real-time adsorption event to monitor protein morphology, a surface based experimental technique will require sub-nanometer resolution and sensitivity for detecting a single molecule. There are several techniques used to study surface adsorption such as quartz crystal microbalance (QCM), surface plasmon resonance (SPR) stimulation, and attenuated total reflectance Fourier transform infrared (ATR-FTIR) spectroscopy. However none of the aforementioned has potential single molecule capability.

My Ph.D. thesis is based on the effort to further develop the WGM sensor. My experimental approach was guided by the theoretical work of Professor Steve Arnold and Professor Iwao Teraoka. In what follows I will describe my journey. First the WGM sensor

will be introduced along with a discussion of its unprecedented sensitivity (Chapter 2). In Chapter 3, I will describe the design and assembly of the WGM sensor. In Chapter 4, I will investigate the resonance frequency shift of the WGM sensor as various nanolayers are added to the microsphere surface, and compare the theory and experiments. I will demonstrate the use of two wavelengths to measure the thickness of a soft-condensed bio-layer. In Chapter 5, I will study protein nanolayers using the WGM sensor and discuss the molecular weight sensitivity of the sensor. In Chapter 6, I will describe polarization effects of WGMs (i.e., transverse electric TE mode and transverse magnetic TM mode). I will investigate TE and TM shift differences by demonstrating the polarization specific stimulation of resonances. Furthermore, I will discuss the possibility of studying a molecular orientation at the silica surface using the TE and TM mode measurements.

Chapter 2

The WGM Sensor

2.1 Optical Resonances and Silica Microspheres

Dielectric microspheres are known to confine light by total internal reflection. Light waves circumnavigate the circumference of the microsphere and continue traveling when light comes back to the origin in phase (Fig. 2A). This condition is known as a whispering gallery mode (WGM) and happens at particular frequencies. A microsphere can support multiple modes; different numbers of waves can fit in the circumference.

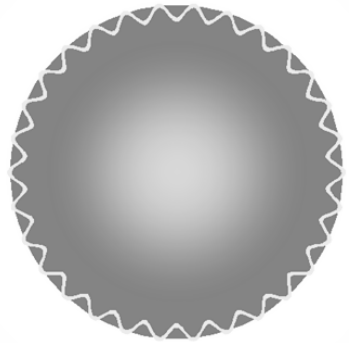

Fig. 2A Whispering Gallery Mode; 30 waves wraps around the circumference of the microsphere.

Fused silica is known for low light absorption at frequencies in the near infrared. Therefore, silica microspheres can confine light for a long period of time. The number of oscillations for which a free oscillator "rings" before losing 67% of its energy is defined as the quality factor $Q/2\pi$. The formal definition for Q is

$$Q = 2\pi \frac{\text{energy stored}}{\text{energy dissipated per cycle}}. \qquad (2.1)$$

The highest Q ever reported for a silica microsphere is $\sim 10^{10.5}$ My advisor, Stephen Arnold, predicted that a silica microsphere would be extremely sensitive to changes in the environment and predicted that a sub-nanometer biomolecular layer should be easy to detect from the frequency shift of a high-Q WGM.[6] The minimum thickness which can be detected is inversely proportional to Q. A quartz crystal microbalance (QCM) has this property in common with the WGM sensor, but the Q of QCM is much smaller, $\sim 5 \times 10^{4}$.[7] An optical

resonance of a silica microsphere achieves a Q nearly 6 orders of magnitude higher.[2] Unfortunately, Q alone does not tell the whole story. The QCM detects molecules through an inertial effect, whereas the WGM sensor utilizes a dielectric perturbation. A silica microsphere should be a superior sensor. How do we know that?

2.2 High-Q Resonances and Sensitive Detection

High Q means that a system has a long lifetime, τ. In time domain, the amplitude of the oscillator is described by the equation, $S(t) \propto e^{-t/2\tau} \mathrm{Sin}(\omega_0 t)$. Fig. 2B shows two systems with τ = 10 s (bold) and 100 s (thin).

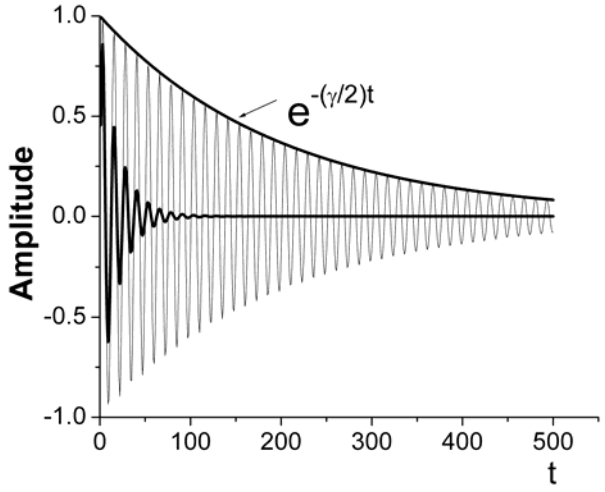

Fig. 2B Time domain plot of two oscillators with τ = 10 s (bold) and τ =100 s (thin). γ is the rate at which the energy decays (i.e. γ =1/τ).

From Fourier relations, we learn that time and frequency domains are conjugates. In frequency domain, a damped system can be represented by a power spectrum of the form $S(\omega) \propto \frac{1}{(\omega - \omega_0)^2 + \left(\frac{\gamma}{2}\right)^2}$. Fig. 2C is the frequency domain plot. We notice that the oscillator having the slower damping has the narrower width.

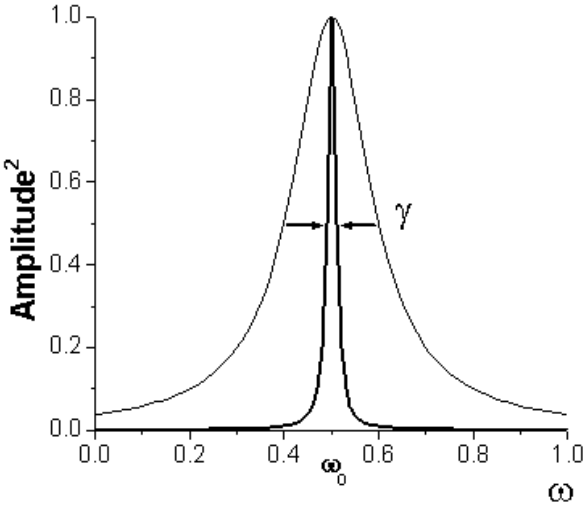

Fig. 2C Frequency domain plot of two oscillators with $\gamma = 0.1\ s^{-1}$ (thin) and $\gamma = 0.01\ s^{-1}$ (bold).

High-Q silica microspheres have large τ values. Therefore they have extremely narrow linewidths (small γ). Q in terms of resonant frequency and linewidth is,

$$Q = \frac{\omega_0}{\gamma}. \qquad (2.2)$$

If we are to detect molecules by looking at a shift of the resonance frequency, the linewidth should be very small. A narrow width allows us to measure a small change in frequency with greater resolution (see Fig. 2D).

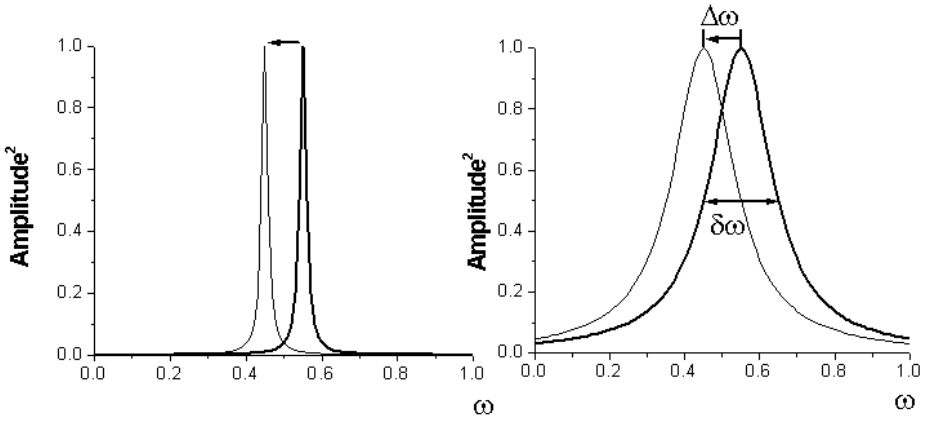

Fig. 2D Schematic representation of frequency shifts with two linewidths: $\gamma = 0.01\ s^{-1}$ (left) and $0.1\ s^{-1}$ (right).

A ~100 μm radius silica microsphere with Q of 10^6 confines photons for 1 ns. In 1 ns, light travels ~0.3 m. If we use 1300 nm laser, the linewidth of the resonance will be 1.3 pm. Common spectroscopic techniques in analytical chemistry describe their resolution by the term spectral bandwidth, which is defined as full width at a half of full height. The typical bandwidth is 0.1 to 1 nm. A silica microsphere has much smaller bandwidth, leading to a much greater resolution.

If we make a conservative estimate that the smallest shift $\Delta\omega$ we can measure is the full linewidth $\delta\omega$, what is the sensitivity? Imagine molecules adsorbing onto the surface and forming a thin layer. Assuming the molecules have the same dielectric properties as silica, the silica microsphere radius R will increase by the layer thickness t (Fig. 2E).

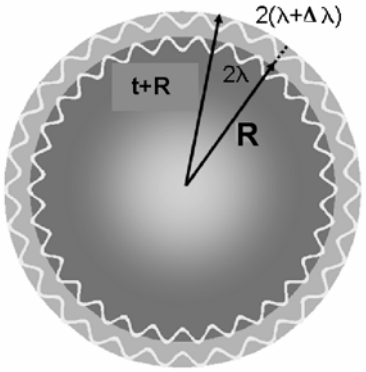

Fig. 2E Change in wavelength due to the microsphere radius increase.

Since the product of the microsphere radius and the wave vector of a given mode is constant, the wavelength has to increase in order to accommodate the radius change. We have a simple relationship:

$$\frac{\Delta\lambda}{\lambda} = \frac{t}{R}. \qquad (2.3)$$

For a modest Q = 10^6, R= 100 μm, and λ= 1300 nm, the thickness of the layer we can see is 1 angstrom! We can easily detect a biomolecular layer, since the size of typical biomolecule is 1nm.

2.3 Theoretical Approach: Quantum Analog

An image of photons circumnavigating close to a microsphere surface resembles an electron orbiting around the nucleus in a hydrogen atom. Using the quantum analog, we can take the advantage of similarities in the two systems and avoid exhaustive mathematics of electromagnetism to understand the characteristics of WGMs.

By revisiting the hydrogen atom and understanding how the effective potential energy traps the electron in its potential well, we can visualize how a photon gets trapped inside the potential well of a microsphere in WGMs.

In quantum mechanics, the energy of a hydrogen atom (its reduced mass, μcan be calculated by the time-independent Schrödinger equation $\hat{H}\psi = E\psi$ where $\hat{H} = -(\hbar^2/2\mu)\nabla^2 + V(\mathbf{r})$ and $V(\mathbf{r})$ is the Columbic potential, $-q^2/\mathrm{r}$. We can combine V and E terms and obtain

$$\nabla^2\psi + (2\mu/\hbar^2)\left[E - V(\mathrm{r})\right]\psi = 0. \tag{2.4}$$

Constructing the Laplacian using the dimensionless angular momentum operator, $\hat{L} = -i(\vec{\mathrm{r}} \times \nabla)$; we obtain $\nabla^2 = \left(\frac{1}{\mathrm{r}}\frac{\partial^2(\mathrm{r})}{\partial \mathrm{r}^2} - \frac{\hat{\mathrm{L}}^2}{\mathrm{r}^2}\right)$. Replace the Laplacian and multiply each term with r, Eqn. 2.4 becomes

$$\frac{\partial^2(\mathrm{r}\psi)}{\partial \mathrm{r}^2} - \frac{\hat{L}^2(\mathrm{r}\psi)}{\mathrm{r}^2} + \frac{2\mu}{\hbar^2}\left(E + \frac{q^2}{\mathrm{r}}\right)\mathrm{r}\psi = 0. \tag{2.5}$$

We separate the wavefunction $\psi(\mathbf{r})$ into radial and angular components,

$$\mathrm{r}\psi(\mathbf{r}) = \psi_r(\mathrm{r})\mathrm{Y}_{\ell,m} \tag{2.6}$$

and use

$$\hat{L}^2\mathrm{Y}_{\ell,m} = \ell(\ell+1)\mathrm{Y}_{\ell,m} \tag{2.7}$$

where ℓ is the angular momentum quantum number and $\mathrm{Y}_{\ell,\mathrm{m}}$ is a Spherical Harmonic function with azimuthal quantum number m. With these modifications, Eqn. 2.5 takes the form

$$\frac{d^2\psi_r}{d\mathrm{r}^2} + \frac{2\mu}{\hbar^2}\left[E - \left(\frac{\hbar^2}{2\mu}\frac{\ell(\ell+1)}{\mathrm{r}^2} - \frac{q^2}{\mathrm{r}}\right)\right]\psi_r = 0. \tag{2.8}$$

Fig. 2F shows the effective potential $V_{eff} = \left(\frac{\hbar^2}{2\mu} \frac{\ell(\ell+1)}{r^2} - \frac{q^2}{r} \right)$.

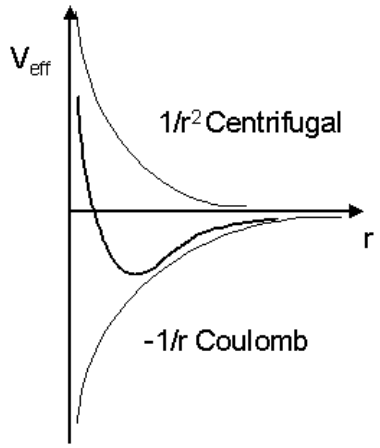

Fig. 2F Effective potential of a hydrogen atom (thick line).

As r approaches infinity, V_{eff} approaches zero. For E>0, a solution of Eqn. 2.8 exhibits an oscillatory behavior at infinity. The solution represents an unbound state, a free electron. For $E<0$, ψ_r has to approach 0 at the two asymptotic limits $r \to \infty$ and $r \to 0$. The function ψ_r takes the form of $\psi_r = e^{-Cr} r^l M(r)$ where $C \equiv \sqrt{-2E/aq^2}$, $a \equiv \hbar^2/\mu q^2$, l = 0,1,2,…, and $M(r) = \sum_{j=0}^{\infty} b_j r^j$. The energy eigenvalues are $-\mu q^4/2n^2\hbar^2$ where n = 1,2,3… The bound-state energy levels of the hydrogen atom energy are discrete.

Photons in a resonant mode have quantized angular momentum just like the electron in the hydrogen atom. In fact, the electromagnetic equations describing the light within a microsphere can be described by a quantum analog known as the Photon Atom Model.[8]

The wave equation which determines the characteristics of WGMs of a microsphere (with no excess charge) has to satisfy the vector Helmholtz equation:

$$\nabla^2 \mathbf{E} + k^2 \mathbf{E} = 0. \qquad (2.9)$$

where **E** is the electric field, $k = \omega n(\mathbf{r})/c$ is the propagation constant and n(**r**) is the refractive index. Applying the same Laplacian, we get

$$\left(\frac{1}{r} \frac{\partial^2 (r)}{\partial r^2} - \frac{\hat{L}^2}{r^2} \right) \mathbf{E} + k^2 \mathbf{E} = 0 . \qquad (2.10)$$

Since $\left[\hat{L}^2,\hat{L}\right]=0$, a solution to Eqn. 2.10 can be written down by examination, $\mathbf{E}=\hat{L}\psi$. This is a so-called TE mode. With this form $\hat{L}$ can be factored through, we obtain Eqn. 2.10 in the form

$$\hat{L}\left[\frac{\partial^2(\mathrm{r}\psi)}{\partial \mathrm{r}^2}-\frac{\hat{L}^2(\mathrm{r}\psi)}{\mathrm{r}^2}+\mathrm{k}^2(\mathrm{r}\psi)\right]=0. \tag{2.11}$$

This vector Helmholtz equation can be satisfied for a finite angular momentum so long as the scalar equation within the brackets in Eqn.2.11 is set to zero;

$$\frac{\partial^2(\mathrm{r}\psi)}{\partial \mathrm{r}^2}-\frac{\hat{L}^2(\mathrm{r}\psi)}{\mathrm{r}^2}+\mathrm{k}^2(\mathrm{r}\psi)=0. \tag{2.12}$$

Eqn. 2.12 can be re-written in the form of a Schrödinger equation using Eqn. 2.6 and 2.7. We add and subtract $\mathrm{k}_0^2\psi_r$ on the left side of Eqn. 2.12.[8] Now Eqn. 2.12 becomes

$$\frac{\mathrm{d}^2\psi_{\mathrm{r}}}{\mathrm{dr}^2}+\{\mathrm{k}_0^2-[\mathrm{k}_0^2(1-\mathrm{n}^2)+\frac{\ell(\ell+1)}{\mathrm{r}^2}]\}\psi_{\mathrm{r}}=0 \tag{2.13}$$

which looks very much like Schrödinger equation with the effective energy k_0^2 and the effective potential

$$\mathrm{V}_{\mathrm{eff}}\left(r;k_0,n,\ell\right)=\mathrm{k}_0^2(1-\mathrm{n}^2)+\ell(\ell+1)/\mathrm{r}^2. \tag{2.14}$$

The first term in the effective potential is negative and leads to dielectric confinement of light, while the second centripetal term is repulsive. The sum of these two terms generates a potential well in which photons can be trapped (see Fig. 2G). To find the resonance position, one has to solve Eqn. 2.13. The solution for a wave function inside the sphere is a Spherical Bessel function. The solution for a wave function outside the sphere is a Spherical Hankel function. Maxwell's boundary conditions demand that logarithmic derivatives of these two functions have to match at the sphere's surface. Detailed electromagnetic calculations were first presented by Gustav Mie near the beginning of the 20th century.[9] Solutions having to do with dielectric perturbations by surface layers have been presented by Folan[10] and Teraoka et al.[11]

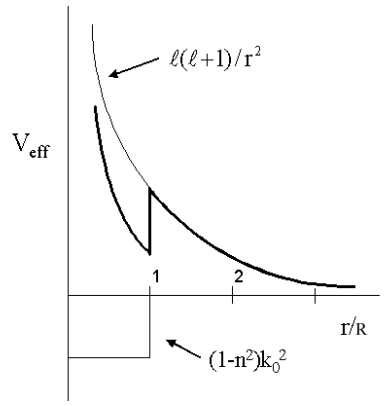

Fig. 2G The effective potential vs. (r/R) for a photonic atom. The sum of $\ell(\ell+1)/r^2$ and $(1-n^2)k_0^2$ terms is shown as the thick line. A pocket formed is the potential well.

2.4 First Order Perturbation Theory

How does the effective potential change when nano-layer adsorb on the sphere surface? Let us use the Photonic Atom approach and perturb the quantum analog potential (Eqn.2.14).[8] The perturbation that the layer causes is:

$$\delta \mathbf{V_{eff}} = \delta\left[\mathbf{k_0^2(1-n^2)}\right]. \tag{2.15}$$

The first order energy shift will be, as in quantum mechanics,

$$\delta \mathbf{E_{eff}} = \frac{\langle \psi_r | \delta \mathbf{V_{eff}} | \psi_r \rangle}{\langle \psi_r | \psi_r \rangle}. \tag{2.16}$$

E_{eff} is k_0^2, so Eqn. 2.16 becomes

$$\delta k_0^2 = \frac{\langle \psi_r | \delta\left[k_0^2(1-n^2)\right] \psi_r \rangle}{\langle \psi_r | \psi_r \rangle}. \tag{2.17}$$

When a layer adds to the surface, what changes is k_0^2 and n^2 in Eqn. 2.17; $\delta(n^2) = n_\ell^2 - n_m^2$, where n_ℓ and n_m are refractive indices of the layer and medium respectively. We can expand Eqn. 2.17 to

$$\delta\left(k_0^2\right)\langle \psi_r | \psi_r \rangle = \delta\left(k_0^2\right)\langle \psi_r | \psi_r \rangle + \langle \psi_r | -k_0^2(n_\ell^2 - n_m^2) | \psi_r \rangle + \langle \psi_r | -2k_0 \delta k_0 n_s^2 | \psi_r \rangle. \tag{2.18}$$

n_s is the refractive index of the microsphere. $\delta\left(k_0^2\right)\langle \psi_r | \psi_r \rangle$ terms drop out and we have

$$\langle \psi_r | -k_0^2(n_\ell^2 - n_m^2) | \psi_r \rangle + \langle \psi_r | -2k_0 \delta k_0 n_s^2 | \psi_r \rangle = 0. \tag{2.19}$$

We deal with a nanoscopic layer on ~200 μm radius, so that we approximate the evaluation of the first term in Eqn. 2.19 using the wave function at the surface.

$$\int_{layer} -k_0^2(n_\ell^2 - n_m^2)|\psi_r|^2 dv \cong -k_0^2(n_\ell^2 - n_m^2)|\psi_r(R)|^2 4\pi R^2 t \qquad (2.20)$$

The second term requires that the integral be evaluated all space. Since at resonance the microsphere contains 94% of the energy within its interior,[12] we evaluate the second term over the interior volume.

$$\int_{\text{all space}} -dv|\psi_r(r)|^2 2k_0\delta k_0 n_s^2 \cong \int_0^R -dr 4\pi r^2|\psi_r(r)|^2 2k_0\delta k_0 n_s^2 \qquad (2.21)$$

From (2.19), (2.20) and (2.21), we obtain the fractional shift in wavelength:

$$\frac{\delta k_0}{k_0} = -\frac{R^2 t\,|\psi_r(R)|^2(n_\ell^2 - n_m^2)}{2n_s^2\int dr\, r^2|\psi_r(r)|^2}. \qquad (2.22)$$

It has been shown that the volume integral in the denominator of Eqn. 2.22 is related to the surface value of the square of the spherical Bessel function for the case where the wavelength is much smaller than the microsphere radius.[13] Therefore, $\int dr\, r^2|\psi_r(r)|^2 = \int_0^R j_\ell^2(\sqrt{\varepsilon_{rs}}k_0 r)r^2 dr \approx \frac{R^3}{2} j_\ell^2(\sqrt{\varepsilon_{rs}}k_0 R)\frac{\varepsilon_{rs} - \varepsilon_{rm}}{\varepsilon_{rs}}$. First order perturbation using the quantum analog gives

$$-\frac{\Delta k_0}{k_0} = \frac{\Delta\lambda}{\lambda} = \frac{(n_\ell^2 - n_m^2)}{(n_s^2 - n_m^2)}\frac{t}{R}. \qquad (2.23)$$

Eqn. 2.23 confirms our simple assumption Eqn. 2.3 and agrees with the calculation of detailed electromagnetic theory for a layer addition in vacuum for a TE mode.[10]

The theory predicts that the shift is proportional to the excess dielectric constant of the layer and its thickness and inversely proportional to the microsphere radius R. Eqn. 2.23 guides our experiments of the WGM sensor. The next chapter describes the sensor setup.

Chapter 3

The WGM Sensor Setup

The WGM sensor consists of six components: a light source, an optical fiber, a sample cell, a detector, a computer for data acquisition and a microsphere. Fig. 3A shows a simple illustration of the sensor.

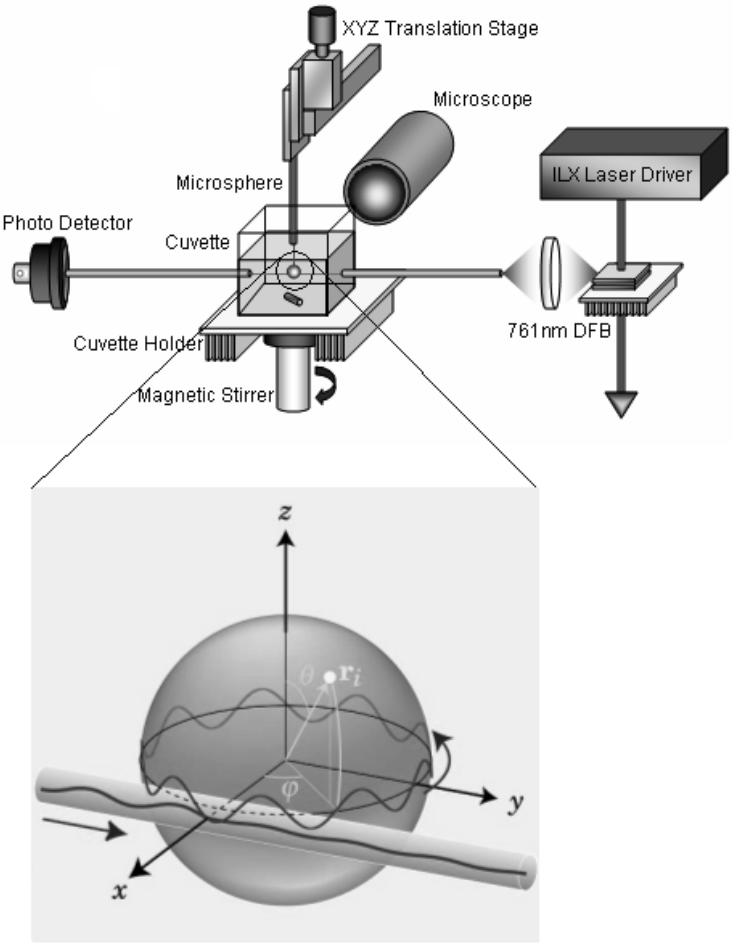

Fig. 3A The basic WGM biosensor set up. A portion of the sample cell is magnified (and rotated by 180º about the z-axis to show the microsphere-fiber coupling).

3.1 Distributed Feedback Laser: A Current-Tunable Light Source

The light source for stimulating WGMs has to meet an important requirement. The

laser itself has to have a very narrow spectral linewidth, narrower than the resonance linewidth of a microsphere. No light source gives a perfectly monochromatic light, yet recent technological advances in telecommunication made our experiments feasible at a reasonable cost. A tunable laser called distributed feedback laser **(**DFB) achieves ~2 MHz (~0.02 pm) spectral linewidth.[14]

The experiments conducted in the this study used two DFB lasers. One is a custom-made 760 nm DFB (Princeton Lightwave) and the other is a 1300 nm pigtailed butterfly laser (NEL America Inc., NLK1B5E1AA). Each laser is mounted on a laser diode mount (ILX Lightwave, LDM-4407). The laser diode controller (ILX Lightwave, 3722B) operates the laser at 25ºC and tunes the laser wavelength by varying the input current. The tuning coefficients of the two lasers were measured using a Michelson interferometer (Advantest, TQ8325). The laser wavelength was measured at 1 mA increment above the threshold. The wavelength dependences are:

$$\lambda_{1300}(\text{nm}) = 1312.438 + 0.0028\,(i,\text{mA}) + (1.55E-5)(i,\text{mA})^2$$
$$\lambda_{760}(\text{nm}) = 761.0185 + 0.0043\,(i,\text{mA}) + (1.003E-5)(i,\text{mA})^2.$$

To scan the laser wavelength, a function generator (HP, 3325A) is used with the ILX controller. The laser current is repeatedly scanned at 2 or 5 Hz typically over the range of 0.06 nm (760 nm laser) or 0.177 nm (1300 nm laser) using a saw-tooth function.

3.2 Optical Circuit

3.2.1 1300 nm DFB laser

A pigtailed laser makes the laser-single mode fiber (SMF) coupling easier. It eliminates hours of focusing the laser light to a SMF. Our 1300 nm laser is pigtailed with a 900 μm buffered SMF and a FC/PC connector at the end. We connect it to a simplex cord (FIS, custom design, Fig. 3B).

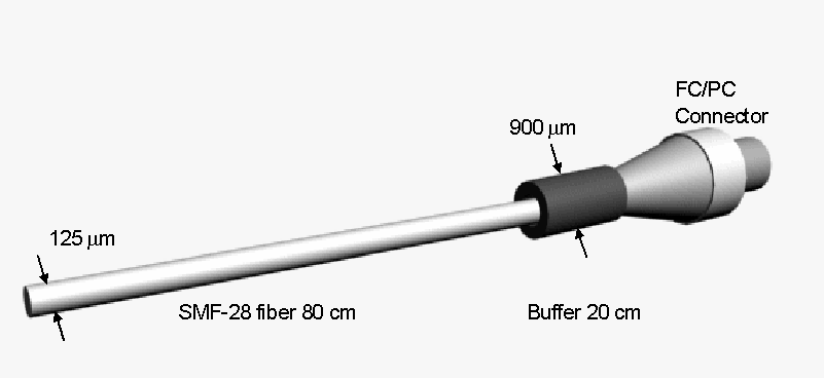

Fig. 3B A simplex cord with a FC/PC connector. The FC/PC end is connected to the pigtailed laser and the bare fiber end is connected to the detector. Not to scale.

This method achieves reproducible laser light coupling with almost no loss (less than 0.3 dB). The optical isolator (Thorlabs Inc., 4013SAFC) can be placed in between the laser and the simplex cord to reduce the back reflection noise.

3.2.2 760 nm DFB laser

The custom-made 760 nm DFB is not pigtailed and hence requires a different optical set up. Fig. 3C shows the details. The light is focused by the mini lens (Thorlabs Inc., 350390-B), and the beam is passed through the optical isolator (Optics for Research, IO-D-780). These two components are housed inside a Teflon piece, which resembles a small ice-hockey pack. The light then is focused to a SMF (Neufurn, 780HP), by a microscope objective lens.

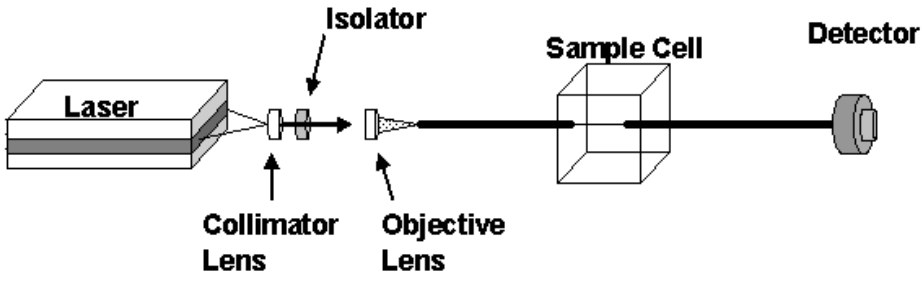

Fig. 3C The optical set up for the 760 nm DFB laser. The collimator lens and the isolator are housed inside a Teflon piece (1" diameter and 1/2" thick). The 780 HP bare fiber is passed through the cuvette and secured by epoxy as described in Chapter 3.4.

3.3 Optical Fiber

Whether it is 760 nm or 1300 nm fiber, the core of the optical fiber needs to be exposed, so that a microsphere can be stimulated into resonance by evanescent coupling. To eliminate the cladding, an SMF fiber is etched in a 20% (v/v) hydrofluoric acid (HF) solution (A146-1, Fisher Scientific).[15]

The fiber etching procedure is described below.

A. Remove the polymer coating from a SMF by applying paint remover (Star Bronze Co., Zip-Strip, contains methylene chloride, ethanol, and methanol) ~5 mm section. Wipe off the paint remover after 5 min. The polymer coating peels off very easily.
B. Clean the exposed section with ethanol.
C. Fill the sample cell with the HF solution, enough to immerse the fiber completely. The fiber diameter should read 125 μm.
D. When the fiber diameter is ~ 4 μm and the intensity reading is 1/3 of the initial reading, stop the etching by removing the HF solution, and rinse the sample cell and the fiber with deionized water. This step takes approximately 4 hours.

Step A and B should be carried out before assembling the SMF and the sample cell.

3.4 Sample Cell

A simple polystyrene cuvette for fluorescence spectroscopy is used for a sample cell. The cuvette is cut to a height of 1.5 cm and an 8 mm diameter hole is removed from its bottom by melting the polystyrene with a hot metal rod. This hole will be replaced with a heat sink plate as a last step in the cell fabrication procedure. Two holes drilled through the side walls accommodate the prepared SMF. The SMF is fixed with an epoxy resin. After etching the fiber, a stainless steel heat sink is epoxied to the cuvette bottom to complete the sample cell.

3.5 Detector

For our 1300 nm laser, an InGaAs photo diode (Thorlabs Inc., PDA500) is used. Light from the 760 nm laser is most efficiently sensed using a silicon photo diode (Newport, 818SL). Wavelength multiplexing experiments are conveniently designed using only the InGaAs detector. Although its sensitivity is considerably less at 760 nm, it is convenient to use one detector for these experiments (see Chapter 4.5).

3.6 Data Acquisition

Detector signals are converted to digital signals and stored in a desktop computer through a DAQ card (National Instrument, 6036E). The LABVIEW program interfaces the data acquisition process. The program displays the transmission spectrum (intensity reading vs. scan wavelength) at typically 0.17 x 10^{-3} nm resolution (1000 points total in a scan) and locates resonance dip positions by a parabolic minimum fit using 11 to 25 points (depending on Q values). The time trace of the resonance positions is recorded. Fig. 3D is a typical transmission spectrum. Stimulated resonances are detected as dips in the spectrum.

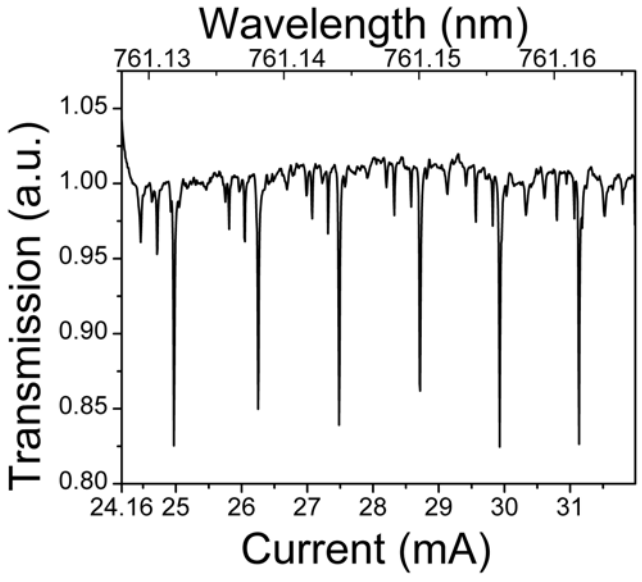

Fig. 3D Transmission spectrum recorded using 760 nm laser. The scan range is 0.04 nm (8mA). The width of a Lorenzian-shaped dip is 0.12 pm and Q is 6 x 10^6. Resonance coupling is about ~20% efficiency.

3.7 Microsphere

A short strip of a SMF is melted in a butane/nitroxide flame (Microflame). The fiber is slowly rotated in the flame to facilitate a spherical bead formation. A typical microsphere is shown in Fig. 3E.

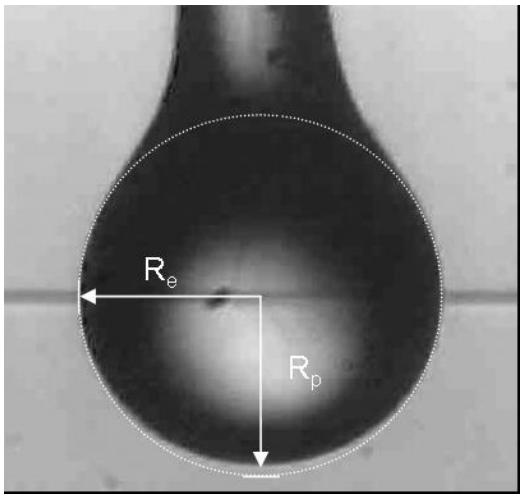

Fig. 3E Optical image of a fabricated silica microsphere. R_e = 204 μm.

Fabricated microspheres are not completely spherical and rather oblate with the radii ratio r_p/r_e ~0.958.

Chapter 4
Study of Nanolayer Adsorption:
Layer Characterization by Wavelength Multiplexing of a Microsphere

4.1 Soft Condensed Bio-Layers

Soft condensed layers made of biological molecules can be formed on glass surface. Protein chips are sophisticated examples of such bio-layers used for gene analysis[16] and drug screening.[17] Biologists treat a glass slide with dextran or poly-L-lysine (PLL) to immobilize cells to study them under the microscope. These bio-molecules and biopolymers may be physically adsorbed or chemically cross-linked to the glass surface. Such layers typically have a sub-micron thickness. Surface plasmon resonance (SPR)[18] and ellipsometry[19] are common techniques employed in layer characterization. We are interested in applying our WGM sensor to characterize such bio-layers. We propose that the WGM sensor can provide non-invasive, real-time measurements of layer formation and determine layer thickness and its optical dielectric profile in excess of the water medium. In the following, we will show how the theory guides us to construct experiments and present the result of PLL layer thickness measurements. We have used two wavelengths to stimulate resonances in one microsphere for this experiment. We call this method "Wavelength Multiplexing."

4.2 The Evanescent Field

When analyte molecules reach the vicinity of a microsphere, what happens to them? The microsphere is in resonance. As light circumnavigates near the circumference of the sphere, the electric field builds up within. Outside the microsphere, an exponentially decaying field (i.e. evanescent field) exists. This evanescent field induces a dipole moment in the molecule in excess of the dipole moment of water molecules. The induced excess dipole moment is $\delta\mathbf{p} = \mathbf{p}_m - \mathbf{p}_w$, where $\mathbf{p}_m$ and $\mathbf{p}_w$ are the dipole moments of the analyte molecule and water molecules of the equivalent volume respectively. Given a local field $\mathbf{E}_0(\mathbf{r})$, we can express $\delta\mathbf{p}$ in terms of excess polarizability α_{ex}, $\delta\mathbf{p} = \alpha_{ex}\mathbf{E}_0(\mathbf{r})$. This energy of interaction perturbs the energy of the resonant state.[4] Therefore we observe the frequency shift of a

WGM when analyte molecules interact with the evanescent field. Outside the evanescent field, analyte molecules will simply not be detected by the microsphere. In other words, the field length determines the sensing depth.

In Chapter 2, we derived the fractional wavelength shift based on the first order perturbation theory. Eqn. 2.23 is shown below.

$$\frac{\Delta\lambda}{\lambda} = \frac{\left(n_\ell^2 - n_m^2\right)}{\left(n_s^2 - n_m^2\right)}\frac{t}{R} \tag{4.1}$$

The shift is proportional to the dielectric property of the layer in excess to the medium and its thickness. This equation is valid if the entire layer is immersed in the evanescent field. We would like to have a more general analytical expression, which can be applied to any layer adsorption studies. We begin by obtaining the expression for the evanescent field.

4.3 The Evanescent Field Length

We constructed a Schrodinger-like equation to describe photons in a resonant mode in Chapter 2. Solving Eqn. 2.13 for outside the microsphere will give us the expression for the evanescent field. We recall Eqn 2.13 as

$$\frac{d^2\psi_r}{dr^2} + \{k_0^2 - [k_0^2(1-n^2) + \frac{\ell(\ell+1)}{r^2}]\psi_r = 0. \tag{4.2}$$

We set n to n_m for the outside and replace r by R (microsphere radius) because the evanescent field decays so rapidly that we only need to consider a small distance from the microsphere surface.

$$\frac{d^2\psi_r}{dr^2} + [n_m^2 k_0^2 - \frac{\ell(\ell+1)}{R^2}]\psi_r = 0 \tag{4.3}$$

Eqn. 4.3 has two exponential solutions; the one with a negative exponent, $-\sqrt{\frac{\ell(\ell+1)}{R^2} - n_m^2 k_0^2}\, r$, allows the photon probability density to decay as one moves radially away from the surface, whereas the other would allow the probability to exponentially increase. For the photon energy which is originally confined, only the former exponent is physical (i.e. the probability of finding photons further out cannot be increasing). From the electric field $\mathbf{E} = \hat{L}\psi$, and Eqn. 2.6, $\psi(r) = \frac{\psi_r(r)}{r} Y_{\ell,m}$, we find the field:

$$\mathbf{E}(\mathrm{r}) \approx A \frac{\exp\left(-\sqrt{\frac{\ell(\ell+1)}{\mathrm{R}^2} - \mathrm{n}_\mathrm{m}^2 \mathrm{k}_0^2}\ \mathrm{r}\right)}{\mathrm{r}} \hat{L}\, \mathrm{Y}_{\ell,m}. \qquad (4.4)$$

A is the constant for the field amplitude at the microsphere surface. Approximating $\sqrt{\ell(\ell+1)} \sim \ell + 1/2$ and taking the k_0^2 outside,

$$\mathbf{E}(\mathrm{r}) \approx A \frac{\exp\left(-\mathrm{k}_0 \sqrt{\left(\frac{\ell+1/2}{\mathrm{k}_0 \mathrm{R}}\right)^2 - \mathrm{n}_\mathrm{m}^2}\ \mathrm{r}\right)}{\mathrm{r}} \hat{L}\, \mathrm{Y}_{\ell,m}. \qquad (4.5)$$

For an infinitely large ℓ, $\mathrm{n_s k_0 R} \approx \ell + 1/2$. However ℓ is not infinitely large. We define the ratio $\mathrm{n_{eff}} \approx \frac{\ell + 1/2}{\mathrm{k_0 R}}$ and use the formulation developed by Lam et al.[20], which enables us to estimate $\mathrm{n_{eff}}$ for a large ℓ. For very large values of ℓ, it can be shown that $\mathrm{n_{eff}}$ approaches $\mathrm{n_s}$.[12] Eqn. 4.5 becomes

$$\mathbf{E}(\mathrm{r}) \approx A \frac{\exp\left(-\mathrm{k}_0 \sqrt{\mathrm{n}_\mathrm{s}^2 - \mathrm{n}_\mathrm{m}^2}\ \mathrm{r}\right)}{\mathrm{r}} \hat{L}\, \mathrm{Y}_{\ell,m}. \qquad (4.6)$$

We are interested in the relative evanescent field intensity just beyond the surface. Since the field at the surface is $\mathbf{E}(\mathrm{R})$, we find that

$$\left|\frac{\mathbf{E}(\mathrm{r})}{\mathbf{E}(\mathrm{R})}\right|^2 \approx \exp\left(-2\mathrm{k}_0 \sqrt{\mathrm{n}_\mathrm{s}^2 - \mathrm{n}_\mathrm{m}^2}\,(\mathrm{r} - \mathrm{R})\right)\left(\frac{\mathrm{R}}{\mathrm{r}}\right)^2. \qquad (4.7)$$

The characteristic length $\mathrm{L_c}$ for the intensity to fall to 1/e from the surface value is

$$\mathrm{L_c} = \frac{1}{2\mathrm{k}_0 \sqrt{\mathrm{n}_\mathrm{s}^2 - \mathrm{n}_\mathrm{m}^2}}. \qquad (4.8)$$

$\mathrm{L_c}$ for 1300 nm and 760 nm wavelengths are ~165 nm and ~97 nm respectively. Fig 4A shows the evanescent field intensity profile for the two wavelengths.

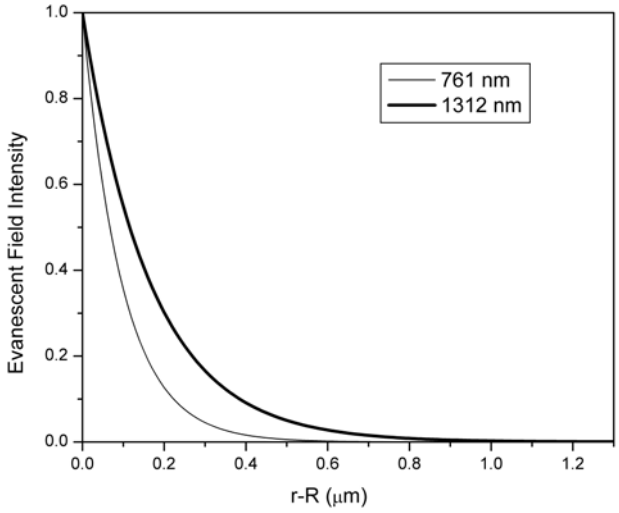

Fig. 4A The evanescent field intensity profile from the sphere surface to radial distance r. The surface evanescent intensity is taken as 1.

The characteristic length in each case is about one eighth of the respective wavelength. This implies that the resonance shift can be used as a sort of "nanoscopic ruler". It is clear from the Fig. 4A that bio-molecules at 500 nm from the surface will have a greater influence on a resonance stimulated at 1300 nm than they do on the one excited at 760 nm.

4.4 The General Form of the Fractional Wavelength Shift

We are ready to combine our understanding of the evanescent field and the result of the first order perturbation theory, Eqn. 4.1. However before proceeding, it should be pointed out that Eqn 4.1 assumes that the refractive index of the layer n_ℓ is constant (or homogenous) within the layer. It is hard to imagine that a layer, which consists of bio-molecules or biopolymers, has a perfectly uniform distribution of molecules within the layer. Imagine that polymer chains are attached to the microsphere and each chain extends outward from the surface. The polymer segment density will be the highest at the surface and will decrease as you move away from the surface. It is more realistic to think that the refractive index within the layer has a characteristic distribution. We call $n_\ell^2(r) - n_m^2$ distribution the excess dielectric profile, κ_e, extending from r = R.

We apply κ_e and correct for the evanescent field. Eqn. 4.1 becomes

$$\frac{\Delta\lambda}{\lambda} = \frac{1}{R(n_s^2 - n_m^2)} \int_R^\infty \kappa_e(r - R)\, e^{-(r-R)/L} dr \qquad (4.9)$$

where L is the wavelength dependent evanescent field length. For those familiar with Laplace transforms it will be apparent that the shift is proportional to the LaPlace transform of the excess dielectric profile. To render Eqn 4.9 more familiar we set $\xi = r - R$ and evaluate the integral from the surface to the thickness t:

$$\begin{aligned} \frac{\Delta\lambda}{\lambda} &= \frac{(n_\ell^2 - n_m^2)}{(n_s^2 - n_m^2)} \frac{1}{R} \int_0^t e^{-\xi/L} d\xi \\ &= \frac{(n_\ell^2 - n_m^2)}{(n_s^2 - n_m^2)} \frac{L}{R} \left[1 - e^{-t/L}\right] \end{aligned} \qquad (4.10)$$

For the case of very thin layers (t/L << 1), we can approximate Eqn. 4.10 by taking the Taylor expansion of $\left[1 - e^{-t/L}\right]$term. We recover our familiar Eqn. 4.1.

$$\frac{\Delta\lambda}{\lambda} = \frac{\left(n_\ell^2 - n_m^2\right)}{\left(n_s^2 - n_m^2\right)} \frac{t}{R} \text{ (for t/L <<1)} \qquad (4.11)$$

The general form, Eqn. 4.9, is shown to be consistent with the other equations in our preceding discussion. The goal here is to measure and characterize a PLL layer. There are two unknowns in Eqn. 4.11: n_ℓ and t. Using two wavelengths to measure$\Delta\lambda/\lambda$, we will have two equations.

4.5 Two-Wavelength Measurements

Using 760 nm and 1300 nm lasers, we will obtain

$$\begin{aligned} \left(\frac{\Delta\lambda}{\lambda}\right)_{760} &= \frac{(n_\ell^2 - n_m^2)}{(n_s^2 - n_m^2)} \frac{L_1}{R} \left[1 - e^{-t/L_1}\right] \\ \left(\frac{\Delta\lambda}{\lambda}\right)_{1300} &= \frac{(n_\ell^2 - n_m^2)}{(n_s^2 - n_m^2)} \frac{L_2}{R} \left[1 - e^{-t/L_2}\right] \end{aligned} \qquad (4.12)$$

If we assume that the leftmost factor on the right hand side of the Eqn. 4.12 does not depend on λ, we can eliminate the factor by taking the ratio of the two equations above. Table 1 lists the refractive indices of water and glass at 760 and 1300 nm regions at 20ºC.

Table 1. Refractive indices of water and silica.

Wavelength (nm)	Water	UV grade fused silica
786	1.32888(*21)	1.45356(22)
1300	1.3210(*21)	1.44692(22)

*measured at 768.2 nm and 1256 nm.

Generally the refractive index of a material increases, as the wavelength becomes shorter. Carbonatious materials also follow this trend. Consequently, with respect to the shift as expressed in Eqn. 4.10, our assumption that the ratio, $\left(n_{\ell}^2 - n_m^2\right)/\left(n_s^2 - n_m^2\right)$, is relatively independent of wavelength between 768 nm and 1300 nm in Eqn. 4.10 in comparison to the evanescent factor, $\mathbf{L}(\lambda)\left[1 - \mathbf{e}^{-\mathbf{t/L}(\lambda)}\right]$ appears sound. On this basis the ratio of fractional shifts allows us to reasonably cancel out the dielectric factor.

We define the ratio of $(\Delta\lambda/\lambda)_{760}$ and $(\Delta\lambda/\lambda)_{1310}$ as S:

$$S = \frac{\left(\frac{\Delta\lambda}{\lambda}\right)_{760}}{\left(\frac{\Delta\lambda}{\lambda}\right)_{1310}} = \frac{L_1}{L_2}\frac{\left[1 - e^{-t/L_1}\right]}{\left[1 - e^{-t/L_2}\right]}. \qquad (4.13)$$

Eqn. 4.13 is simple. It serves as a guide for designing our surface layer analysis method. For an ultra thin layer (i.e., t/L_1, $t/L_2 << 1$), S approaches 1, whereas for a thick layer (i.e., t/L_1, $t/L_2 >> 1$), S approaches L_1/L_2, which with n_{eff} taken constant is λ_1/λ_2. For our chosen wavelengths, this ratio is 0.58. In between the two extreme cases, S falls off in an approximate exponential fashion with a characteristic length $t_c \sim 192$ μm (i.e., $S \approx \left(L_1 / L_2\right) + \left(1 - L_1 / L_2\right)\exp(-t / t_c)$, see Appendix 1) (Fig. 4B).

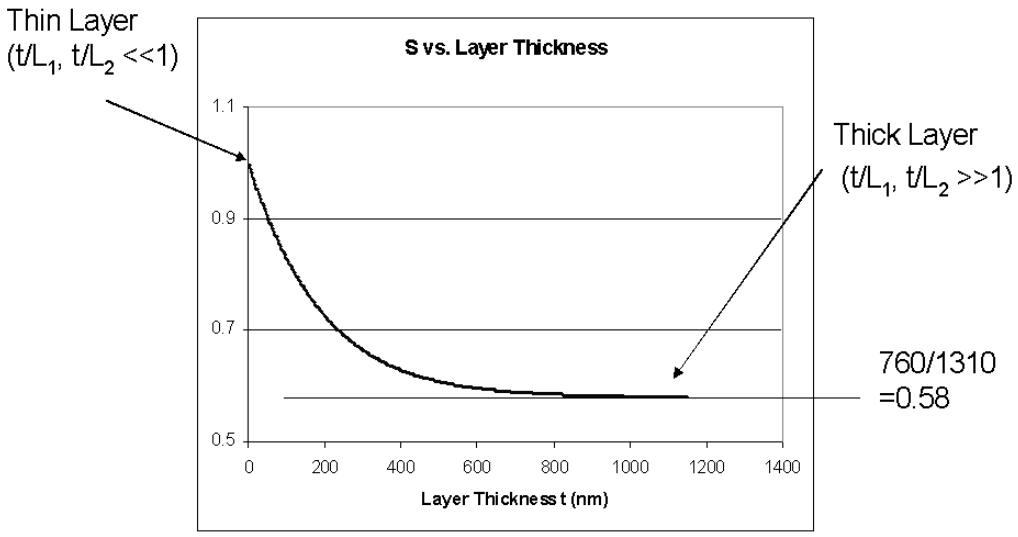

Fig. 4B S, the ratio of $(\Delta\lambda/\lambda)_{760}$ and $(\Delta\lambda/\lambda)_{1310}$, against layer thickness t.

Measuring S allows us to estimate t. With t in hand, we can find the excess refractive index of the layer from Eqn. 4.12.

4.6 Experimental Approach

To measure wavelength shifts for the two light sources, we used an evanescent coupler (Canadian Instrumentation and Research Limited, Serial # 5547-1). 760 nm and 1310 nm lasers were connected to the coupler inputs (Fig. 4C).

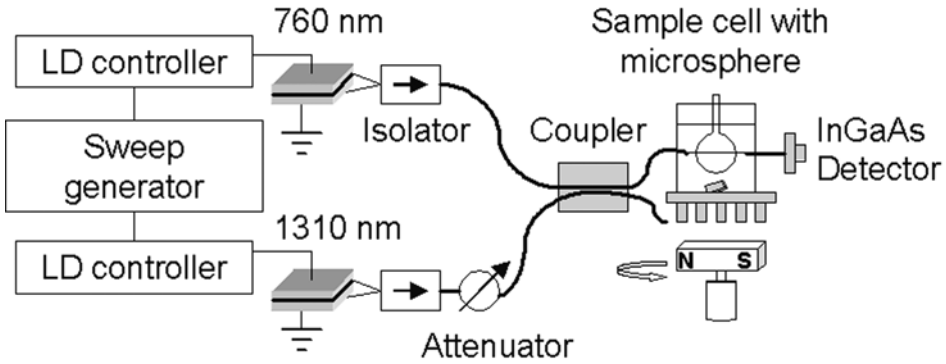

Fig. 4C Experimental set up for wavelength multiplexing of a microsphere.

One of the coupler outputs was connected to a single-mode fiber (Nufern, 780-HP). The fiber and the sample cell were prepared and assembled as described in Chapter 3. The lasers were scanned with a synchronous ramp. A microsphere was stimulated into resonance by mechanical contact with the eroded fiber, and the transmission light intensity was monitored with the InGaAs detector.

We observed that the light from each laser independently stimulates WGMs in the microsphere and yields a distinct transmission spectrum with superposition of resonant dips from each. By observing which resonance dips disappear as either light is shut off, the individual resonances can be easily associated with the 760 or 1310 nm region. Fig. 4D shows the resonance spectrum from the 760 nm laser only (left) and the spectrum with resonance dips from the two lasers (right). A new resonance from the 1310 nm laser can be unambiguously identified.

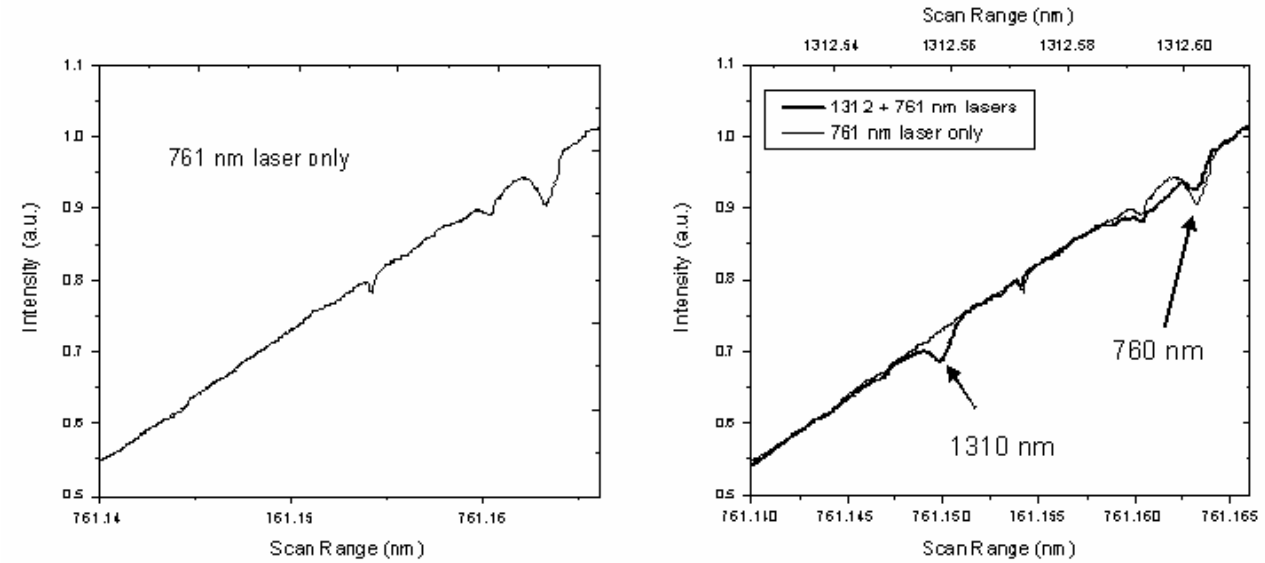

Fig. 4D Transmission spectrum of the 760 nm laser (left) and the superposition of resonances from the two lasers (right).

We take advantage of a frequency domain measurement. This approach enables us to use one microsphere to measure the shifts at two wavelengths while keeping all the experimental conditions identical.

4.7 Verification of Two Limiting Cases

We recall from Fig. 4B; the ratio S approaches 1 for an ultra thin layer and 0.58 for a thick layer. We constructed two experiments to verify these two limiting cases of S. For an ultra thin layer, we chose Bovine Serum Albumin (BSA). BSA layer on a counter-charged silica surface is about 3 nm in thickness.[23,24] For the other limit, we used sodium chloride (NaCl) to increase the refractive index of the sample cell solution homogeneously. This uniform change in the refractive index is considered an infinitely thick layer.

4.7.1 BSA Adsorption Experiment

Albumin is a ubiquitous protein. BSA, albumin in the serum of bovine, has molecular weight ~66,000 g/mol. BSA adsorption onto a surface can be facilitated and enhanced by adjusting the protein solution pH. For this experiment, we adsorb BSA to the surface by electrostatic attraction between the positively charged microsphere surface (amine modified) and the negatively charged BSA molecules.

Protein adsorption is a complex and dynamic phenomenon. Electrostatic protein-protein and protein-surface interactions, hydrophobic interactions, and deformation of protein molecules are considered the key factors to control adsorption processes.[25-28] Protein adsorption and silica surface chemistry will be discussed in detail in Chapter 5.

BSA solution was prepared using a salted phosphate buffer (PBS, 10 mM, pH 7.4, 0.15 M NaCl). The isoelectric point (pI) of BSA is 4.7. At pH 7.4, BSA has net negative charges. On the other hand, the silica microsphere is modified to have amine groups on the surface. Terminal amine ($-NH_2$)'s pKa value is ~8 and it is a basic functional group. The amine group forms $-NH_3^+$ taking a proton from a water molecule.

The Silica surface was acid cleaned and then treated with 3-aminopropyltrimethoxysilane solution (30% v/v in methanol) for 30 minutes. The microsphere was rinsed with methanol and cured at 70ºC for 10 minutes. The microsphere was used immediately after the modification.

The sample cell containing 980 μl PBS was maintained at 25ºC. The sample cell solution was mixed by a magnetic stirring bar. The freshly prepared microsphere was attached on the xyz stage to stimulate WGMs in the sample cell. Once the resonance spectrum was obtained, the LABVIEW program was started to monitor the dip positions. When the baseline stabilized, 20 μl BSA solution was injected into the sample cell with the final BSA concentration being 1μM, and the resonance dip positions were tracked. The adsorption was carried out under constant mixing. The experiment was terminated when the dip positions stopped moving. Fig. 4E is the time trace of the resonance dip positions.

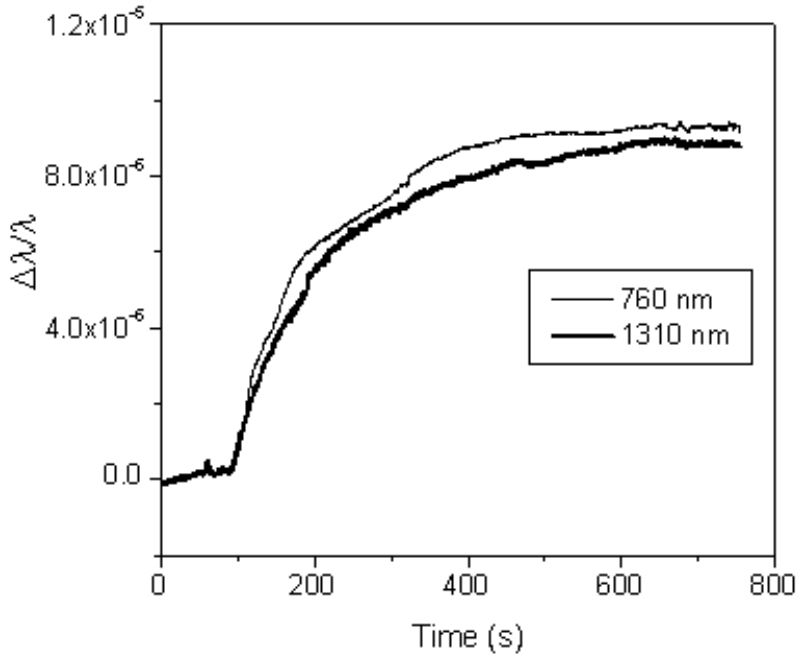

Fig. 4E Resonance shift due to BSA adsorption: Resonance dip from 760-nm laser (thin) and a dip from the 1310 nm laser (bold).

The measured shift is $\Delta\lambda/\lambda \sim 1 \times 10^{-5}$. The two resonances from the two wavelength regions shifted by almost the same amount.

4.7.2 NaCl Experiment

Addition of NaCl to the sample cell increases the refractive index of the solution. With mixing, the solution achieves homogenous $\delta(n^2)$. The microsphere detects the change within the evanescent field length. We expect that the 1310 nm resonance shift more than the 760 nm resonance.

The microspheres used in this experiment were cleaned with the piranha solution (see Appendix 2). 20 µl of 5 M NaCl solution was added to the sample cell containing 900 µl of deionized water. 6 injections were carried out. The salt concentration increased in 0.1 M increment. The sample cell was maintained at 25ºC.

Resonance wavelength shifts for the first two injections are shown in Fig. 4F.

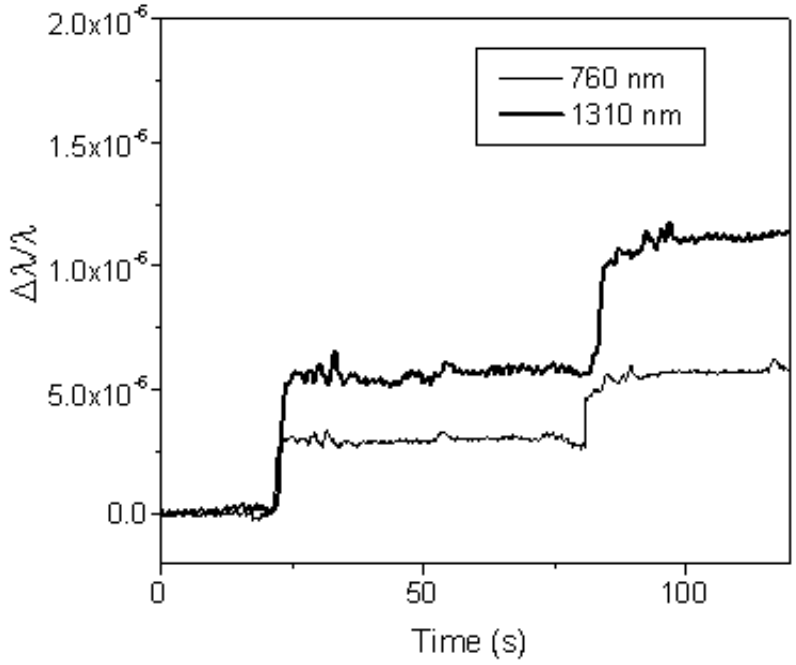

Fig. 4F Time trace of resonance positions, NaCl experiment: 760 nm (thin) and 1310 nm (bold).

Resonance at 760 nm shifted considerably less than that at 1310 nm. We now have the experimental data for the two extreme cases. We would like to know how the measurements compare with our theory.

4.7.3 Theory and Experiment

Fig. 4G summarizes the measurements and the theory. In the plot of $(\Delta\lambda/\lambda)_{760}$ against $(\Delta\lambda/\lambda)_{1310}$, the slope gives the ratio S.

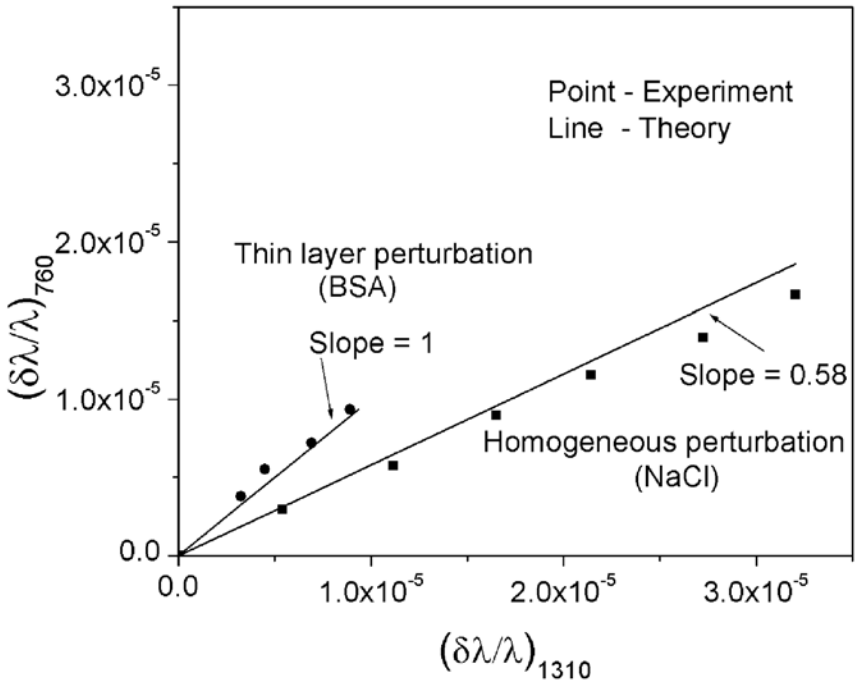

Fig. 4G The plot of $(\Delta\lambda/\lambda)_{760}$ against $(\Delta\lambda/\lambda)_{1310}$. The points represent the actual data; the lines are from the perturbation theory.

For a BSA layer, t/L <<1, and S should approach 1. The experiment yields a slope of 1.04. For the NaCl experiment, t/L >>1, and S should approach the ratio of the wavelengths, 0.58. The experimental result was 0.54.

Our limiting tests are in reasonable agreement with theory. We are now in the position to evaluate the optical properties of soft condensed biolayers.

4.8 Poly-L-Lysine Measurements

Poly-L-lysine is a polypeptide of L-lysine. The structure is shown in Fig. 4H. pKa value of the side group amine is ~10, which is highly basic. The positive charges on the polymer chain provide strong electrostatic interactions.

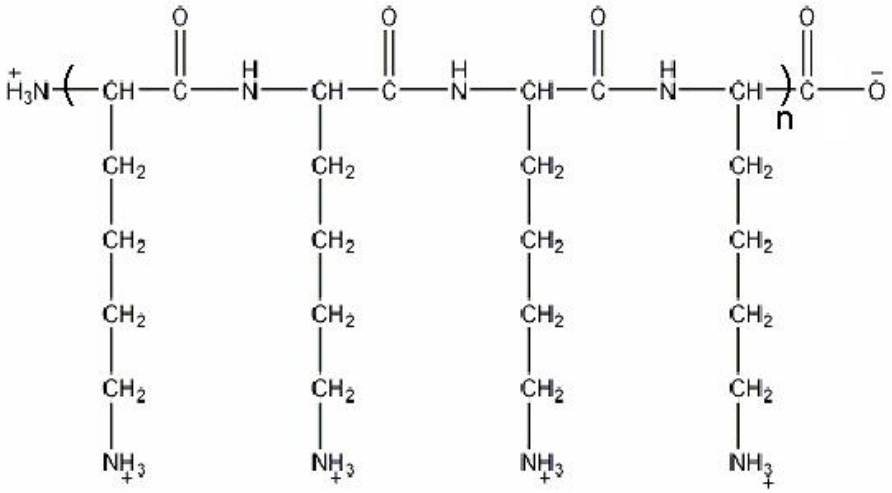

Fig. 4H Structure of PLL. In water ~pH 7, amine and carboxyl groups are predominantly ionized.

Commercially available PLL is in 500 to 300,000 g/mol range. Near pH 7, PLL is known to assume a random structure in solution.[29] However, conformation and orientation of adsorbed PLL chains are not well known. Interestingly, a scanning electron micrograph of a PLL coated silicon wafer shows that PLL produces a uniform smooth surface.[30]

It has been postulated that the electrostatic interactions cause adsorption of polyelectrolyte on oppositely charged surfaces.[31] There are several examples of polyelectrolyte adsorption on counter charged surfaces have been observed.[32,33] SPR has been used in attempt to measure thickness of PLL layers. A PLL layer (average molecular weight 14,000 g/mol) was found to be 1 nm on the self-assembled monolayer of 11-mercaptoundecanoic acid on gold.[18] However the estimation of thickness is based on the bulk refractive index of PLL, 1.52.[18,34]

We measured the resonance shift due to PLL adsorption on an acid cleaned silica microsphere surface (negatively charged; more discussion in Chapter 5). A 40 μl of PLL solution (Sigma, P8920, average molecular weight 225,000 g/mol), which is commonly used to treat glass slides, was injected into a sample cell containing 900 μl PBS. The cell temperature was maintained at 25ºC and the solution was constantly mixed. Fig. 4I is the time trace of resonance dip position at 760 and 1310 nm wavelength.

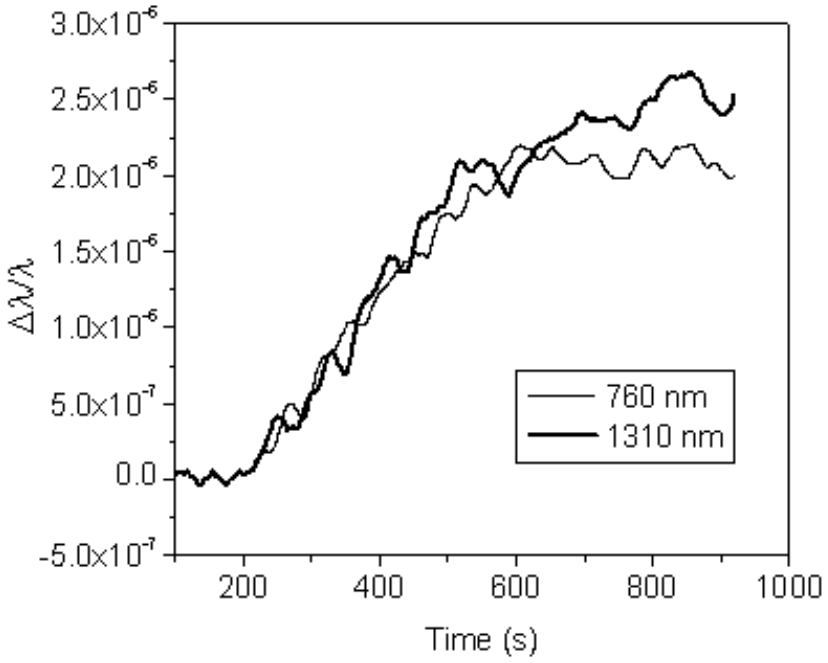

Fig. 4I Resonance shifts due to PLL adsorption onto the silica microsphere. 100-point data smoothing applied.

The adsorption saturated at $\Delta\lambda/\lambda \sim 2 \times 10^{-6}$. The measured shift is extremely small compared to BSA and NaCl experiments. Subsequent injections of the PLL solution did not increase the shift.

Based on four experiments, the average slope S was 0.82. This slope fed back into Eqn. 4.13 gives a thickness of 110 nm. After substituting the thickness into Eqn. 4.12, we determined the excess dielectric constant to be $\delta(n^2) = 0.0033$. Consequently $\delta n = 0.0012$, which is indeed small.

4.9 Conclusions

We have shown that the WGM sensor can be used to measure the thickness of an adsorbed bio-functional layer through wavelength multiplexing of a microsphere. We find that a PLL layer has extremely low contrast to a water environment.

We verified Eqn. 4.10 in the two limits. We were, therefore, in a good standing to apply our first order perturbation theory to layer analyses.

The PLL experiments give some insights into the structure of PLL chains within the layer. From the average molecular weight of PLL, the fully extended chain length as a rigid rod is roughly 770 nm. Our measured thickness 110 nm may suggest that the polymer chains are not adsorbed end-on, normal to the surface.

Using the bulk refractive index of PLL, the effective volume occupied by PLL polymers in the layer is estimated as 0.6%. Polymer chains are not tightly bound to the surface lengthwise, and they do not pile up on top of each other to achieve ~100 nm thickness. It is more likely that the polymer chain touches the surface at several points along the chain, so that flexible and free parts of the chain occupies a certain volume within the "layer structure" (Fig. 4J). Polymer chains are highly dispersed and the layer does not have a tight rigid structure.

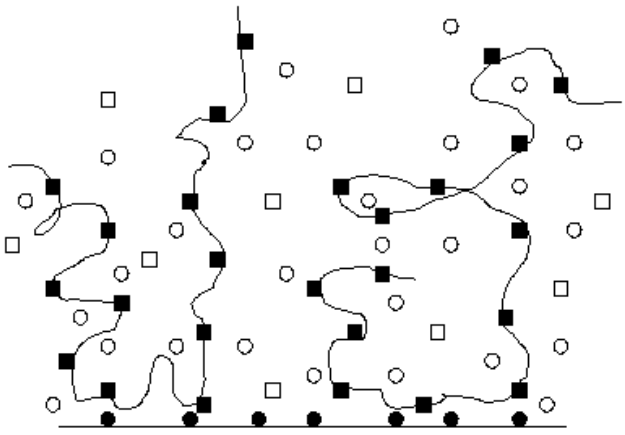

Fig. 4J Illustration of a possible PLL chain arrangement near the surface. ■ is the positive charge on the polymer chain. ● is the surface negative charge. ○ and □ are ions in the solution.

How does the edge of such polymer layer look like? Since the polymers are loosely held together and highly dispersed within the layer, the refractive index of the layer cannot abruptly reduce to the refractive index of the surrounding at the edge of the layer. In other words, the edge of the layer must be very fuzzy. In Chapter 4.4, we made an assumption that $\kappa_e = n_\ell^2 - n_m^2$. We assumed the sharp boundary of a PLL layer. Can we obtain a real spatial profile of the excess dielectric constant experimentally?

We propose that we can use the WGM sensor to profile a layer edge by multiplexing more than two wavelengths. We call this idea "evanescent sounding". As shown in Appendix 1, we obtained the function of S by taking the Laplace transform of a step function. We think that the excess dielectric profile κ_e in Eqn. 4.9 can be determined by taking an inverse Laplace transform of the wavelength shift data at multiple $\Delta\lambda$s. More points will allow us to profile a soft layer structure in details.

The next chapter will discuss protein layer adsorption studies and molecular weight dependence of the frequency shift of the WGM sensor.

Chapter 5
Molecular Weight Dependence of the WGM Sensor

5.1 Thin Protein Layer Analyses

We have verified that for formation of an ultra thin layer, a wavelength shift of the WGM sensor does not depend on the wavelength used to stimulate resonances. Having confirmed Eqn. 4.11, we would like to study protein layers in more details.

The estimated number of protein-coding human genes is ~24,500.[35] It will be an exhausting task to study each protein molecule with the WGM sensor. However, protein molecules are macromolecules made of 20 different amino acid residues. Although each protein has a unique amino acid sequence, dielectric properties of proteins are expected to be similar because the building blocks are the same. We are interested in studying how the protein size (i.e., molecular weight) influences the wavelength shift of the WGM sensor.

5.2 Protein Interactions at Solid Surfaces

We describe an adsorption process by looking at the interaction between a protein molecule and a surface binding site (i.e., one-to-one reactions). Proteins in solution bind to surface sites, and the binding can be physical or chemical. Given a protein concentration [A] in moles per litter and the number of surface binding sites N, the rate of adsorption, R_a, is given as[36]

$$R_a = k_a [A](1-\theta)N \qquad (5.1)$$

where k_a is a rate constant for the adsorption and θ is a fraction of the sites occupied. The rate is proportional to how often molecules visit the surface (i.e., the concentration) and the number of available sites. The rate of desorption, R_d, is proportional to the number of occupied sites:

$$R_d = k_d \theta N . \qquad (5.2)$$

k_d is a rate constant for the dissociation. When R_a equals R_d, the two processes have reached the equilibrium. From Eqn. 5.1 and 5.2, we find

$$\theta = \frac{k_a[A]}{k_d + k_a[A]} = \frac{K_e[A]}{1 + K_e[A]}. \qquad (5.3)$$

K_e, the equilibrium constant, is k_a/k_d. This simple adsorption model is known as a Langumir isotherm.[37] The model assumes that all binding sites are uniform and that an occupied site does not affect the binding condition of neighboring sites. One-to-one reactions set the saturation to monolayer formation.

The Arrhenius equation relates two rate constants with temperature T as $k_a \propto \exp(-E_{a,a}/R_{gas}T)$ and $k_d \propto \exp(-E_{a,d}/R_{gas}T)$, where R_{gas} is the gas constant and $E_{a,a}$ and $E_{a,d}$ are the activation energies for adsorption and desorption, respectively. Then K_e depends on T as

$$K_e = \exp\left(-\left(E_{a,a} - E_{a,d}\right)/R_{gas}T\right) = \exp(-\Delta H/R_{gas}T) \qquad (5.4)$$

where ΔH is the enthalpy change.

For many biochemical processes, association and dissociation between substrate and enzyme, or between antigen and antibody, regulate biological functions. If an analyte has high affinity for a ligand, K_e is large and the ligand binding is thermodynamically favored because $E_{a,a} < E_{a,d}$ (see Fig. 5A). Analyte-ligand interactions can be studied using ligands immobilized on a solid surface. Analyte binding can be detected by monitoring the dielectric property change near the ligand surface. The WGM sensors and SPR sensors are such examples.

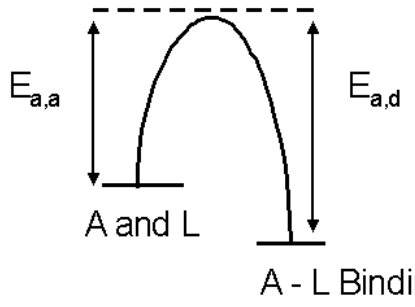

Fig. 5A Energy diagram of analyte A and ligand L in the bound state (right) and unbound state (left). $E_{a,a}$ is the activation energy for association, and $E_{a,d}$ is for dissociation.

In case of physical adsorption of protein onto a solid surface, covalent bonds are neither broken nor formed. Protein-surface binding, yet, needs to be thermodynamically favored. What are the factors, which influence protein-surface binding interactions?

5.3 Factors Controlling Protein Adsorption

Protein purification by chromatography takes advantage of protein – surface interactions. Some medical devices are rendered biocompatible by coating the devices with biomolecules. We find many examples of protein – surface interactions, although it is not yet possible to predict the interaction quantitatively based on protein structure and surface and solution properties.[38]

The adsorption process is known to be extremely sensitive to pH, temperature, ion concentrations and the presence of other molecules.[39] Binding forces can be electrostatic, van der Waals, hydrogen bonding, or combinations of these. Experimental studies show that molecular surface structures affect protein binding[40] and protein undergoes some structural change upon adsorption.[41] Protein – protein interactions also become important as the protein density increases on the surface. The existence of many different equilibrium states has been suggested.[41]

Because of the complexity of protein adsorption, it is important for our molecular weight study to have well-controlled experimental conditions. Microsphere surface modification must be reproducible, so that variations in the amount of protein adsorbed from one microsphere to another are minimized.

5.4 Silica Surface and Modification Methods

Silicon dioxide, a.k.a. silica, is an essential material for many industries, from semiconductor to consumer products. Silica can be natural or synthetic, amorphous or crystalline. The building block of silica is SiO_4 tetrahedron, and sharing of two oxygen atoms per unit gives a chain, three oxygen atoms a sheet and four oxygen atoms a three-dimensional network. Crystalline silica has regular packing of $[SiO_4]^{-4}$ unit whereas amorphous silica has random packing.[42]

Optical fiber is made of synthetic fused silica and is amorphous. As we fabricate a microsphere by melting the optical fiber, we are interested in amorphous silica surface structure. The silica surface structure is known to have several different types of silanol groups (SiOH) (Fig. 5B).

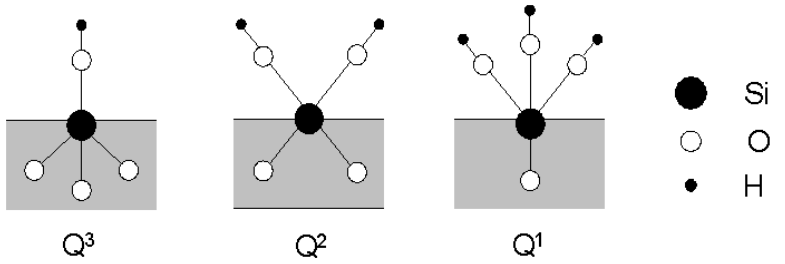

Fig. 5B Schematic representation of surface SiOH groups. The gray portion represents the bulk silica structure. Q^3: Single silanol, Q^2: Geminal, and Q^1: Silanetriol.

Solid-state ^{29}Si NMR is used in surface structure analyses. Q^n terminology is often used where n indicates the number of oxygen atoms linked to the center silicon atom forming the silicon oxide network. For a fully hydroxylated amorphous silica surface, the number of OH groups per square nanometer is 4.6, known as silanol number.[42] A NMR study on silica gel reports the ratio of $Q^2/Q^3/Q^4$ = 9.3/51.8/38.8.[43] The majority of the surface is the single silanol.

Silica surfaces acquire a negative charge in contact with water because of the dissociation of silanol groups.

$$SiOH \underset{\leftarrow}{\longrightarrow} SiO^- + H^+. \qquad (5.5)$$

The extent of this dissociation is characterized by

$$\frac{[H^+]\Gamma_{SiO^-}}{\Gamma_{SiOH}} = K_{SiOH}. \qquad (5.6)$$

Γ is the surface density of chargeable sites. pK_{SiOH} is estimated to be 7.5.[44] 6.8±0.2 and 7.2 are also reported based on the titration study[45] and the IR spectroscopy[46] respectively. Charge surface density of colloidal amorphous silica surface is ~ 0.06 OH^- charges /nm^2 (particle diameter = 15 nm, NaCl concentration = 0.1N, pH = 7).[47] The negative charge on the surface can facilitate the adsorption of positively charged molecules by electrostatic attraction.

Reacting the surface with a silane coupling agent or coating the surface with a polymer solution can modify a silica surface. Chemical modifications often work by replacing the X group of a silane coupling agent with a new O – Si bond of the surface silanol (Fig. 5C).

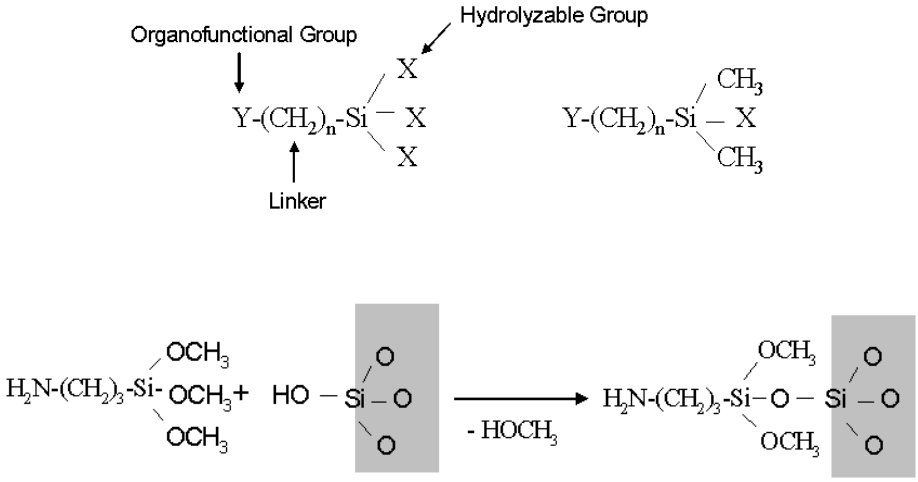

Fig. 5C Top: Typical silane coupling agents: tri-functional (left) and mono-functional (right). Bottom: General reaction scheme for 3-aminopropyltrimethoxysialne and silica surface.

Various silane coupling agents are commercially available. Y group can be monoamine (H_2N-), carboxylate (HOOC-), halogen ($ClCH_2$) and many others. Linker length may vary up to n = 10. X group is typically alkoxy or halogen. If the silane coupling agent has three X groups (trialkoxy), the reacted silanes can cross-link with the neighbors (Fig. 5D).

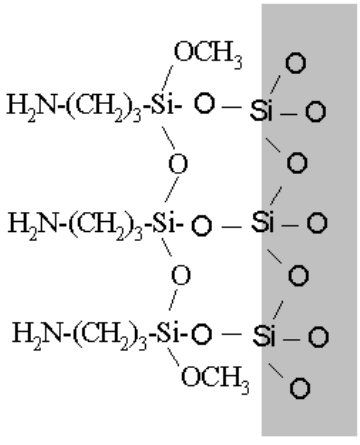

Fig. 5D Cross-linking between adjacent silane coupling agents.

Surface modification by coating takes advantage of negative charges on the silica surface or the hydrogen bonding capability. PLL and dextran are commonly used for coating.

For our molecular weight study, the silica microspheres are modified with 3-aminopropyltrimethoxysilane. The reaction is carried out in solution. Detailed surface modification procedures used in the experiments are summarized in Appendix 2. Based on IR spectroscopy measurements of four porous silica particle samples modified using the same method, this solution-based procedure is verified for its reproducibility. 17±3% of surface silanol groups are replaced by aminopropyl functionalities.

With the understanding of protein adsorption behaviors and with the silica surface modification method in place, our goal is to vary the molecular weight (MW) of the protein samples, measure the resonance shift by monolayer coverage for each sample, and look for the correlation between the shifts and molecular weights.

5.5 Molecular Weight Dependence Experiments

5.5.1 Protein Sample Preparation

Five water-soluble globular proteins are selected from molecular weight 5,000 to 700,000 g/mol (Table 2).

Table 2. Molecular weight and isoelectric point of five proteins.

Protein	Molecular Weight (g/mol)	Isoelectric Point (pI)
Insulin bovine pancreas	5,800	5.3
α-Lactalbumin	14,300	5.1
Bovine serum albumin	66,000	4.8
γ-Globulin bovine	152,000	7.2
Thyroglobulin bovine	670,000	4.6

All proteins except γ-globulin have pI below 7. These proteins are negatively charged at pH 7.4, which is ideal for the positively charged amine microsphere surface. Therefore, these

proteins are dissolved in 10mM PBS (pH 7.4 and 150 mM NaCl) to make up stock solutions at desired concentrations.

γ-Globulin has pI 7.2. At pH 7.4, γ-globulin is close to neutral and its affinity for the amine surface is expected to be weaker compared to the other proteins. To optimize the protein – surface interaction, pH of the PBS solution is set to 6 instead of 7.4 and the microsphere surface is modified to carboxyl functional groups. Under this condition, γ-globulin is positively charged whereas the surface is negatively charged. A stock solution of γ-globulin is prepared using 50 mM PBS (pH 6, 150mM NaCl).

5.5.2 Adsorption Experiments

The WGM sensor setup as described in Chapter 3 is used. The 760 nm DFB laser is used as the light source. All adsorption experiments are carried out at 25º C under constant mixing. A freshly prepared amine or carboxyl microsphere is used for each experiment. Each experiment is carried out according to the procedure described below. After each experiment, the sample cell is rinsed with ethanol then deionized water to minimize build-up of protein molecules.

The adsorption experiment protocol:

A. Add a 980 μl PBS solution to the sample cell.
B. Attach a freshly modified microsphere to the xyz stage and bring the sphere in contact with the etched optical fiber in the sample cell. Obtain a stable resonance spectrum (i.e., dips in the transmission spectrum).
C. Monitor the resonance positions. Allow the microsphere to equilibrate with the sample cell temperature.
D. When the time trace of the resonance position is stable, 20 μl of a protein stock solution is injected into the sample cell.
E. Protein adsorption is monitored until no further shift of resonance is observed.

Fig. 5E shows the resonance spectra from 0.18 μM γ-globulin injection experiment.

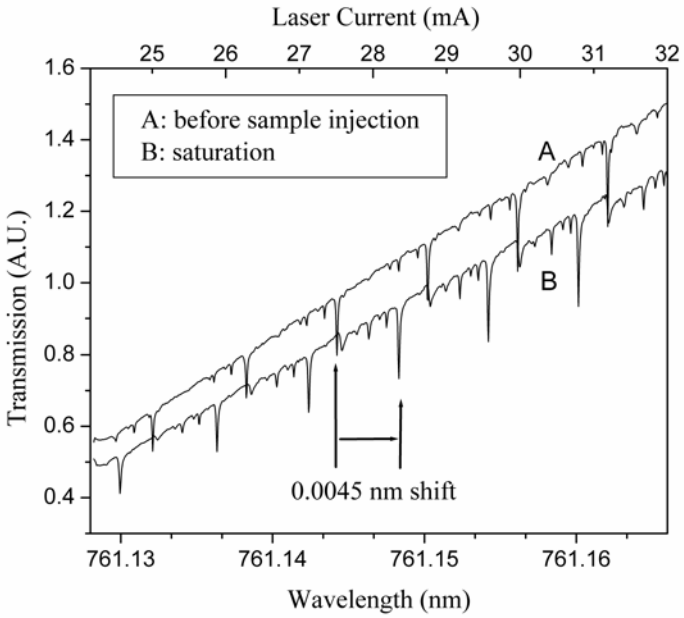

Fig. 5E Transmitted light intensity as a function of the laser current recorded in a γ-globulin experiment; A: the spectrum right before the protein injection, B: the spectrum at the end of the experiment. The positive ramp is due to the higher laser power output for the larger current input.

The spectrum A was recorded right before the sample injection and the spectrum B recorded after 35 min when the adsorption reached equilibrium. γ-Globulin adsorption onto the carboxylated microsphere surface at 0.18 μM concentration in 50 mM PBS (150 mM NaCl, pH 6) resulted in a red shift of the resonance wavelength, 0.0045 nm. The equilibrium was reached ~30 minutes after the injection.

The decrease in light intensity from spectrum A to B is due to a slight adsorption of protein molecules to the optical fiber. The optical fiber is made of silica. Silica acquires a negative charge in water. γ-Globulin is attracted to negatively charged surfaces under this experimental condition. So it is not surprising that γ-globulin sticks to the fiber as well as the microsphere. The decrease in the light intensity was not observed in the experiments with other proteins.

Fig. 5F is the time trace of resonance dip positions from two independent experiments. The thick line is the shift due to 0.93μM γ-globulin injection and the dotted line

is from 0.18μM γ-globulin injection. The initial kinetics and the final level clearly depend on the concentration of the protein.

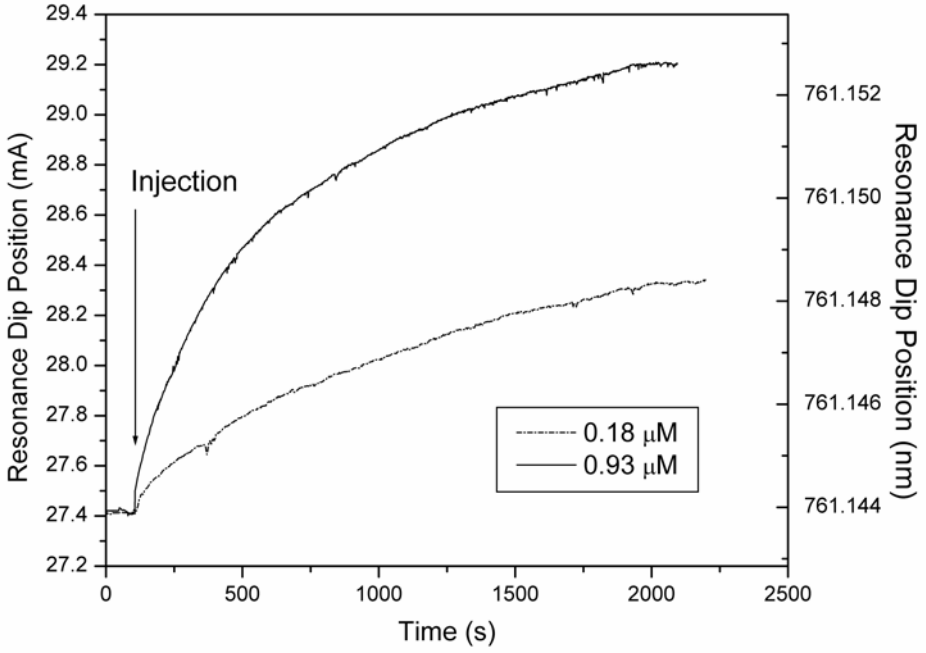

Fig. 5F Resonance dip position vs. time. γ-Globulin adsorption onto carboxylated microsphere surface at 0.93μM (thick line) and 0.18 μM (dotted line) concentrations.

To obtain the wavelength shift at the full saturation level for each protein sample, adsorption isotherm was studied. BSA, α-lactalbumin, and thyroglobulin isotherms are shown in Fig. 5G. The wavelength shift $\Delta\lambda/\lambda$ is inversely proportional to a sphere radius R. Each experiment uses a different size sphere; therefore each point is multiplied by R for the plot.

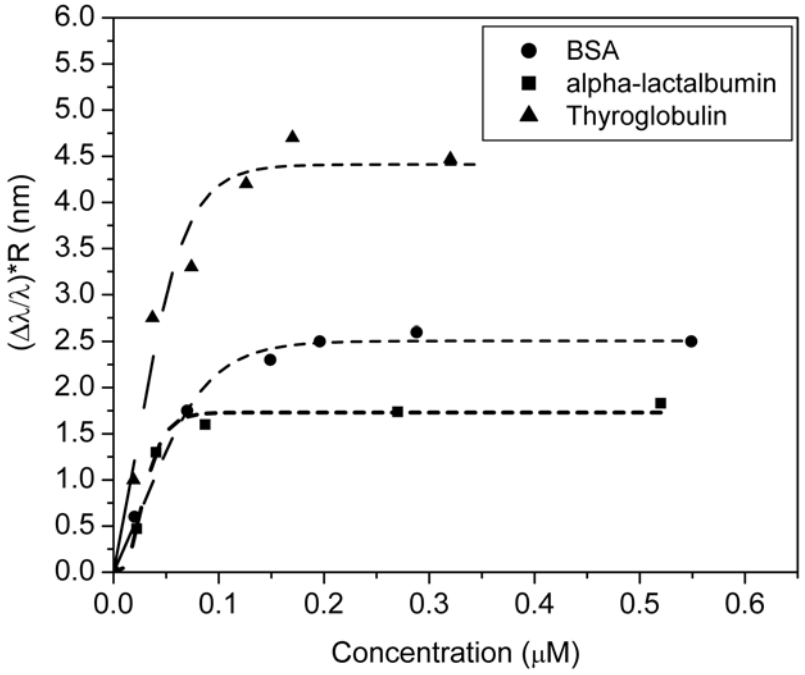

Fig. 5G Adsorption isotherm of α-lactalbumin ( ), BSA ( ), and thyroglobulin ( ). The dotted lines are to guide your eyes.

All five proteins follow a Langumir-like adsorption isotherm, suggesting a monolayer level surface saturation. α-Lactalbumin, BSA, and thyroglobulin reach the monolayer saturation at around 0.15 μM whereas insulin and γ-globulin required 0.5 nM and 4.3 μM, respectively. The concentration required to achieve the maximum surface coverage is thus found for each protein. Adsorption experiments were repeated at the full saturation concentration. Fig. 5H summarizes the wavelength shifts due to the monolayer formation for the five proteins.

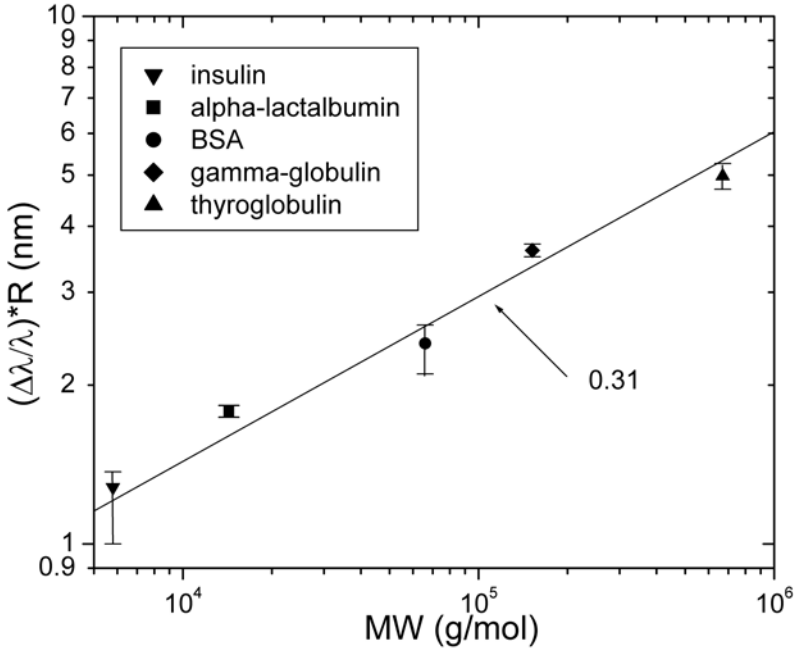

Fig. 5H Resonance wavelength shifts against protein molecular weight in a double logarithmic scale. The data are the average of three measurements. The line was drawn manually to fit the data.

The monolayer saturation shifts for the five proteins fall onto a straight line on a logarithmic scale. The slope of the line is 0.31±0.02. We replot the data to determine whether the shift is proportional to $(MW)^{1/3}$. In Fig. 5I, the fit goes through the origin. We confirm that the shift is proportional to the 1/3 power of the protein molecular weight.

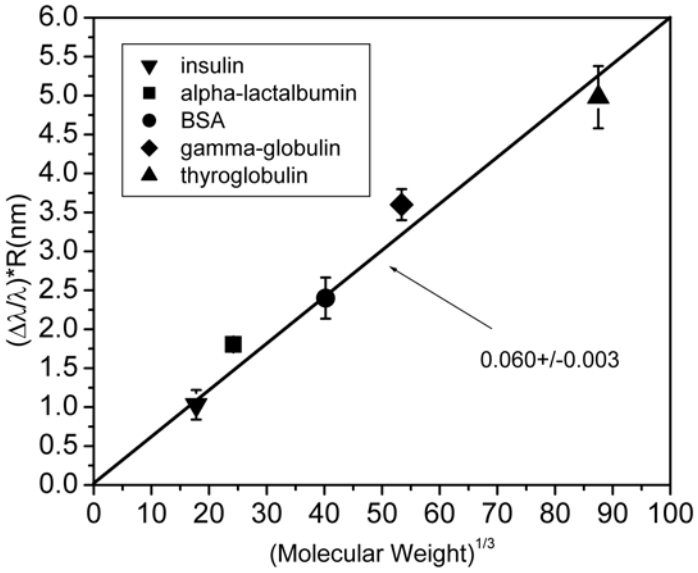

Fig. 5I The measured shifts against $MW^{1/3}$. Error bars show the spread of data from three measurements.

The experiments find that $(\Delta\lambda/\lambda)*R(nm) \approx 0.06\ [MW(g/mol)]^{1/3}$. In Chapter 4, we confirmed that Eqn. 4.11 can be applied to adsorption of an ultra thin layer such as a protein monolayer.

$$\frac{\Delta\lambda}{\lambda} = \frac{\left(n_\ell^2 - n_m^2\right)}{\left(n_s^2 - n_m^2\right)}\frac{t}{R} \qquad (5.7)$$

Can we relate our empirical relation to Eqn. 5.7? Can we provide a physical picture of what 0.06 means? We attempt to answer these questions by proposing a model and apply it to our data.

5.6 Data Interpretations

α-Lactalbumin (LA) is known to have a spherical shape from x-ray crystal structure.[48] Minton modeled LA as a sphere and successfully calculated the monolayer capacity for nonspecific adsorption of LA onto a planer surface.[49] We treat LA as a model spherical protein and interpret the $MW^{1/3}$ dependence of the resonance shift.

The volume of a sphere of radius r is $(4\pi/3)r^3$. Another expression for the volume of a protein molecule is $MW / (N_A \rho_p)$, where N_A is Avogadro's number and ρ_p is protein mass density (practically identical for all proteins,[50] ~1.37 g/cm^3). By equating these two expressions, we obtain the thickness t = 2r in terms of MW:

$$t = 2\left(\frac{3}{4\pi}\right)^{1/3}\left(\frac{MW}{N_A \rho_p}\right)^{1/3}. \tag{5.8}$$

We replace t in Eqn. 5.7 and obtain,

$$\frac{\Delta\lambda}{\lambda} = \frac{\left(n_\ell^2 - n_m^2\right)}{\left(n_s^2 - n_m^2\right)}\frac{2}{R}\left(\frac{3}{4\pi}\right)^{1/3}\left(\frac{MW}{N_A \rho_p}\right)^{1/3}. \tag{5.9}$$

The $MW^{1/3}$ dependence is evident in Eqn. 5.9.

Since protein layers are never 100% protein, we take an effective medium approach for the protein layer. If protein molecules occupy a volume fraction *f* in the layer, the effective dielectric constant $n_\ell^2 = \varepsilon_\ell$ will be given as

$$n_\ell^2 = \varepsilon_\ell \cong f\, n_p^2 + (1-f)n_m^2. \tag{5.10}$$

where $n_p \cong 1.50$ is the refractive index of protein.[51,52] We combine Eqn. 5.9 with Eqn. 5.10 and obtain

$$\frac{\Delta\lambda}{\lambda} = \frac{f\left(n_p^2 - n_m^2\right)}{\left(n_s^2 - n_m^2\right)}\frac{2}{R}\left(\frac{3}{4\pi}\right)^{1/3}\left(\frac{MW}{N_A \rho_p}\right)^{1/3}. \tag{5.11}$$

Our measurements yield $(\Delta\lambda/\lambda) * R(\text{nm}) = 0.06\left[MW(\text{g/mol})\right]^{1/3}$. From Eqn. 5.11, using n_s = 1.46 and n_m = 1.33, we find that the value of f is 0.34 and therefore the effective protein layer refractive index is 1.39. Is 34% reasonable? Based on a rigorous simulation study, Torquato reports that random sequential addition (RSA) of spherical particles to a planer surface achieves the maximum surface area coverage (projection onto the surface) of 0.55 at the jamming limit (i.e., without overlapping spheres).[53] This fractional area coverage equals to the volume fraction of 0.37. Our LA layer on the microsphere surface is close to the theoretical maximum packing density.

The other four proteins we studied are known to assume non-spherical shape. BSA, for example, is heart-shaped.[54] The measured shifts for these non-spherical proteins follow

the $MW^{1/3}$ dependence. A resonance shift of the WGM sensor appears to be insensitive to the shape of a protein molecule.

5.7 Refractive index change in the medium due to the addition of protein

The protein concentration required for monolayer saturation for α-Lactalbumin, BSA, and thyroglobulin is around 0.15 μM. Insulin and γ-globulin require 0.5 nM and 4.3 μM, respectively. The amount of protein added to the medium increases the refractive index of the medium. If there were no protein adsorption onto the microsphere surface, what would be the shift due to the refractive index change in the medium?

The differential refractive index, dn/dc, of a protein in aqueous buffer is typically ~0.18 cm^3/g.[55] Using the highest protein concentration required for γ-globulin, we calculate the refractive index change. For 4.3 μM (6.5×10^{-4} g/ml) of γ-globulin, the solution refractive index increases by 1.2×10^{-4}.

The fractional wavelength shift due to a uniform refractive index in the medium is given by:[11]

$$\frac{\Delta\lambda}{\lambda} = \frac{(\Delta n_m) n_m}{\left(n_s^2 - n_m^2\right)^{3/2}} \frac{\lambda}{2\pi R}. \qquad (5.14)$$

From Eqn. 5.14, $(\Delta\lambda/\lambda)*R$ is 0.13 nm for $\Delta n_m = 1.2 \times 10^{-4}$. The measured shift for γ-globulin monolayer saturation is $(\Delta\lambda/\lambda)*R$ = 3.6 nm. Therefore, the shift due to the refractive index change of the medium is negligible in the experiment with γ-globulin. For the other proteins, the contribution is even smaller.

5.8 Conclusion

We have found that the wavelength shift of the WGM sensor is proportional to the one-third power of protein molecular weight for monolayer saturation. This molecular weight sensitivity offers an advantage for the WGM sensor. Direct electrical detection of biomolecule in field effect transistors cannot provide information on molecular properties such as molecular weight because the signal transduction relies on electrical potential change

due to the presence of analyte molecules. Optical resonance detection directly scales with molecular size.

Our data analysis using α-lactalbumin as a model protein finds that the layer is 34% protein. The volume fraction achieved is close to the theoretical limit for random sequential addition of spherical particles to a planer surface.

Our experiments on PLL and protein layers were measured without identifying the polarization of a resonance mode. In the next chapter, we demonstrate selective stimulation of TE and TM modes. Furthermore, we show that TE and TM measurements may be used to obtain information on the shape and the orientation of an adsorbed protein molecule on the sphere surface.

Chapter 6

Polarization Dependence of Resonance Shifts

6.1 Two Polarizations of Microsphere Resonances

Our discussion in the nanolayer characterization and the molecular weight dependence was based on a transverse electric (TE) mode, one of the two polarizations of a WGM. The Helmholtz equation from which we obtained the TE modes has another independent solution, a transverse magnetic WGM (TM mode).

The TE mode has an electric filed tangential to the microsphere surface. The field of the TM mode is close to normal to the sphere surface (Fig. 6A). The intensity ratio of the tangential component to the normal component of the TM field is roughly estimated as 0.15 for the wavelength, 1.3 μm, and the sphere radius, 200 μm. The ratio is sufficiently small to allow us to consider that the TM mode is polarized predominantly in the normal direction.

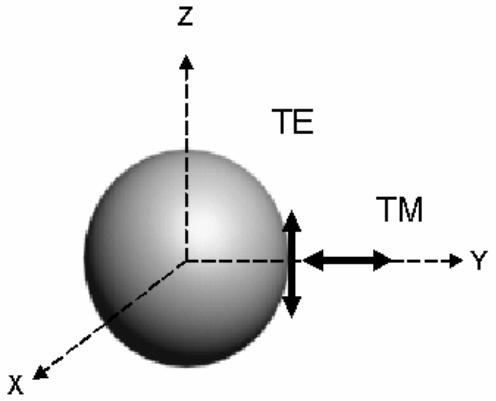

Fig. 6A Field orientations of TE and TM modes.

Lam et al. derived an explicit asymptotic formula for the resonance positions in a spherical microparticle with radius R and refractive index n_s placed in air.[20] We can theoretically calculate resonance positions and the separation between TE and TM modes.

$$n_s x_{\ell,\nu} \approx (\ell + 1/2) + \frac{\alpha_\nu}{2^{1/3}}(\ell + 1/2)^{1/3} - \frac{P}{(n_s^2 - 1)^{1/2}} + \frac{3}{10}\frac{\alpha_\nu^2}{2^{2/3}}(\ell + 1/2)^{-1/3} \qquad (6.1)$$

where $x_{\ell,\nu} = 2\pi R / \lambda_0 = k_0 R$ is a dimensionless size parameter, ℓ is a mode number, α_ν is a root of the Airy function for a mode order *v*, and λ_0 is the wavelength in vacuum. P is n_s for

TE mode and $1/n_s$ for TM mode. A rough estimate of ℓ is $\ell + 1/2 \approx n_s k_0 R$ (see Appendix 3 for more discussion). Table 3 lists TE and TM mode positions for $\nu = 1$ and 2 (α_1=2.338 and α_2 = 4.088).

Table 3. Resonance positions for a sphere of R= 200 μm and n_s=1.47 in air (excitation wavelength λ_0 =1.3μm).

ℓ	ν	λ (TE) μm	λ (TM) μm	Δλ (TE-TM) nm
1400	1	1.300235	1.299564	0.6708
1401	1	1.299315	1.298645	0.6699
1400	2	1.285989	1.285333	0.6562
1401	2	1.285086	1.284431	0.6553

Serpengüzel et al. reported an experiment on polystyrene sphere (R=15 μm) resonance excitation and successfully identified the polarization and the mode order of resonance peaks in the scattering spectrum.[6]

In Table 3 we find that, for a spherical particle, the spacing between resonance positions of adjacent mode numbers but the same mode order is ~0.9 nm. The spacing between TE and TM modes of the same mode number and the same mode order is ~0.7 nm. The resonance spacing is wider than our maximum scan range of ~0.3 nm. We typically observe about 5 dips over the 0.3 nm scan and therefore the spacing is ~0.06 nm. The oblate shape of our fabricated microsphere accounts for this discrepancy. Since our cavity is not spherical, modes of different azimuthal quantum numbers m (m=$-\ell$,.., 0, .., ℓ) are no longer degenerate. For ℓ=1000, the number of states of different m is 2001. They are split into separate modes. By considering the circumference change for Δm=1 for our typical oblate (pole radius/equator radius =0.958), the spacing between resonance dips is estimated as ~0.065 nm, which agrees with our observation.[56]

If we are to identify TE and TM modes from the resonance wavelengths, it will be an exhaustive work for our oblate cavity because of the large number of possible m states. We would like to establish an experimental method to control TE and TM mode excitations and measure their resonance wavelength shifts.

Do TE and TM modes shift by the same amount? We are interested in measuring TE and TM shifts for a protein layer formation and for homogeneous refractive index change in the medium surrounding the microsphere. If TE and TM shifts are not the same, what will be the difference?

Teraoka and Arnold have addressed the TE and TM shift differences for three types of perturbations.[11] The next section will review their theoretical framework, which will guide the experiment of the present thesis.

6.2 TE and TM Shift Differences

We first consider electric fields at the boundary of two media before we look at TE and TM shift equations. As illustrated in Fig. 6A, the electric field of a TM mode oscillates in the equator plane of the microsphere and has a predominantly radial component whereas a TE field oscillates in the meridional plane with no radial component. The boundary conditions require that the tangential component of the electric field and the normal component of the electric displacement be continuous across the boundary.

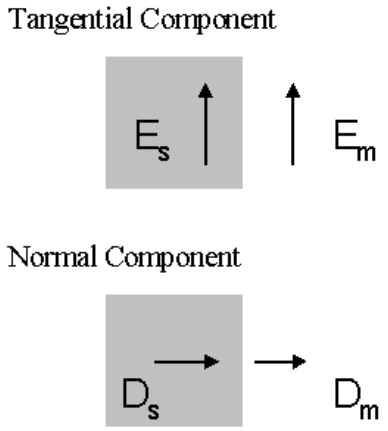

Fig. 6B Electric field at the boundary. Gray blocks indicate the dielectric materials such as silica. E is the electric field and D is the electric displacement.

At the microsphere surface, the field must satisfy $E_s = E_m$ for the tangential component, and $D_s = D_m$ for the normal component. D is related to E as $D = \varepsilon_s E = \varepsilon_0 E + P$ where P is the induced dipole moment per unit volume. To satisfy $D_s = D_m$, the normal component of electric field in the medium must satisfy

$$E_m = \frac{\varepsilon_s}{\varepsilon_m} E_s . \qquad (6.2)$$

For the field normal to the silica/water interface, E_m is larger than E_s by 22%. When the microsphere resonates in the TM mode, the field intensity jumps at the boundary. How does this field jump affect the resonance wavelength shift? Will the stronger field lead to a greater shift?

The estimated resonance wavelength shifts due to a uniform refractive index change in the surrounding medium for a TE mode[11] (see Appendix 4 for details) is,

$$\left(\frac{\Delta\lambda}{\lambda}\right)_{TE} \cong \frac{n_m \Delta n_m}{k_0 R (n_s^2 - n_m^2)^{3/2}} \qquad (6.3)$$

and for a TM mode,[11]

$$\left(\frac{\Delta\lambda}{\lambda}\right)_{TM} \cong \frac{n_m \Delta n_m}{k_0 R (n_s^2 - n_m^2)^{3/2}} \left(2 - \frac{n_m^2}{n_s^2}\right). \qquad (6.4)$$

The ratio of TM to TE shifts is expected to be 1.18.

Protein adsorption presents more complicated issues in estimating the TE and TM shift difference than does the uniform refractive index change. In the early stage of adsorption, protein molecules sparsely cover the microsphere surface. Each molecule interacts with the field independently as if there were no other proteins on the surface. Therefore, protein adsorption at a low density coverage can be treated as single particle adsorption. TM to TE shift ratio of a single particle adsorption is expected to be ~1.2; interestingly it is independent of the refractive index of the particle.[57] When the particle density on the surface is high, it is necessary to consider the effect of nearby particles. Below we consider such an effect.

If we place a dielectric particle in a static electric field $\mathbf{E}_0$, the particle will be polarized (Fig. 6C). The field inside the particle $\mathbf{E}_{internal}$ is smaller than $\mathbf{E}_0$ because of the field due to the induced polarization charges, $\mathbf{E}_{induced}$. When another particle is placed next to this particle, the interaction between the two particles changes $\mathbf{E}_{internal}$ within the two particles. The change is different between the TE and TM modes. For the TM mode, the polarization in the nearby particle decreases $\mathbf{E}_{internal}$ further. For the TE mode, in contrast, the same polarization increases $\mathbf{E}_{internal}$. The TM and TE shift ratio is expected to decrease as the

protein density in the layer increases. The chemical shift in NMR is a good analogy, although it is a magnetic version.

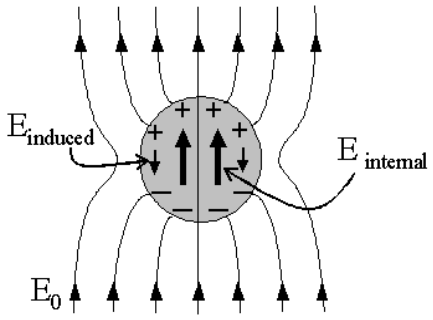

Fig. 6C A dielectric particle in the static electric field E_0.

The effect also depends on the refractive index of the particle. With an increasing refractive index, $E_{internal}$ is further reduced for the TM mode and increased for the TE mode. The magnitude of the change depends on the particle density and the shape of the particle. Fig. 6D compares TM to TE shift ratio for a single particle adsorption and a packed particle layer formation for a particle refractive index value from 1.4 to 1.6.

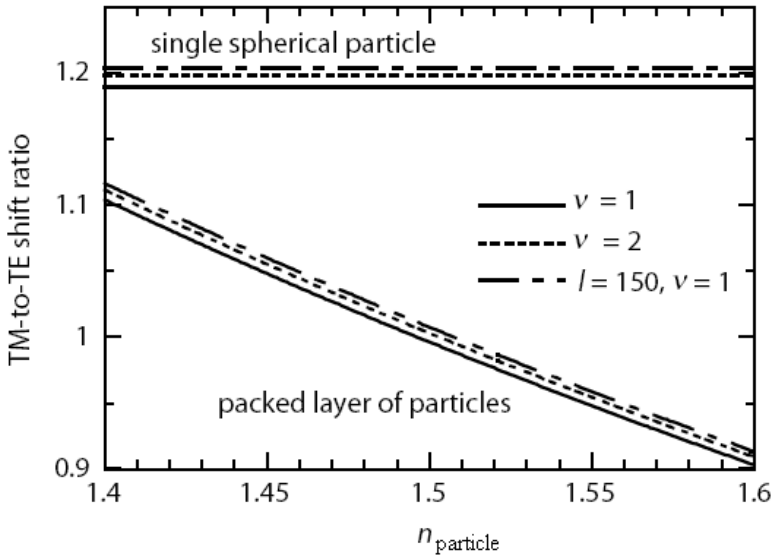

Fig.6D TM to TE ratio of resonance shifts due to a single particle adsorption and a packed sphere layer formation (ℓ = 500 and n_s = 1.47 and n_m = 1.33). ν is a mode order. The figure was adopted from Ref. 57.

The refractive index of a protein molecule is ~1.50. We expect that the ratio will approach 1 for a spherical protein such as α-lactalbumin as more protein molecules are adsorbed.

If the protein shape is not spherical, how does the shape affect TM to TE ratio? Fig. 6E summarizes TM to TE ratios for adsorption of a single protein molecule of various shapes.

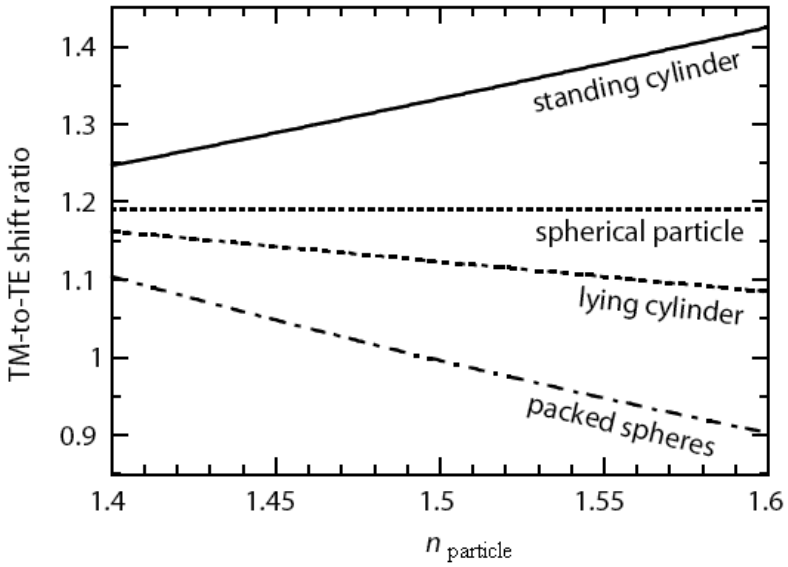

Fig. 6E TM to TE ratio for adsorption of a standing cylinder (line), a lying cylinder (dashed), a sphere (dotted), and a packed layer of spheres (dash-dotted). $\nu = 1$, $\ell = 500$ and $n_s = 1.47$ and $n_m = 1.33$ are used for the calculation. The figure was adopted from Ref. 57.

Polarization-specific shift measurement will give a competitive edge to WGM sensors against SPR sensors. Since SPR can only be excited with p-polarized light, SPR sensors operate with one polarization mode. SPR sensors cannot distinguish a standing rod from a lying rod of the equal volume, for instance.

The TM to TE shift ratio can be interpreted as a measure of the anisotropic polarizability of a molecule. A molecule such as benzene has large anisotropic polarizability. The WGM sensor may be able to distinguish the ring orientation with respect to the microsphere surface by comparing TM and TE shifts.

6.3 Polarization-Specific WGM Stimulation

A laser light is highly linearly polarized. A check with a polarizer reveals that the extinction ratio is nearly 1000 for the pigtailed 1300 nm laser. While keeping the optical fiber as straight as possible and as short as possible, connecting a simplex cord of the sample cell to the laser reduces the extinction ratio typically to ~200. Neither the acid etching of the optical fiber nor mechanical contact of a microsphere with the etched fiber affects the ratio. The linear polarization of the laser light is reasonably conserved from the light source to the detector in the WGM sensor setup.

It was found that the polarization of the light within the optical fiber can be manipulated by rotating the laser mount. When the laser mount is rotated by +10º, the light propagating in the optical fiber also rotates by approximately +10º. Fig. 6F shows the laser rotation arrangement.

Fig. 6F The laser on a rotation stage and the analyzer placed in front of the detector to check the orientation of the light within the optical fiber. The sample cell is omitted for clarity.

For a given orientation of the laser, the analyzer in front of the photodetector was adjusted for the transmission intensity maximum. The laser was rotated by angle ξ, and the analyzer was rotated by θ for the maximum transmission. Fig. 6G is a plot of θ as a function of ξ. The data are on a straight line of $\theta = \xi$, indicating that the polarization of the light within the optical fiber rotates with the laser. The linearity of the polarization does not change as the extinction ratio was held at ~200 for all angles.

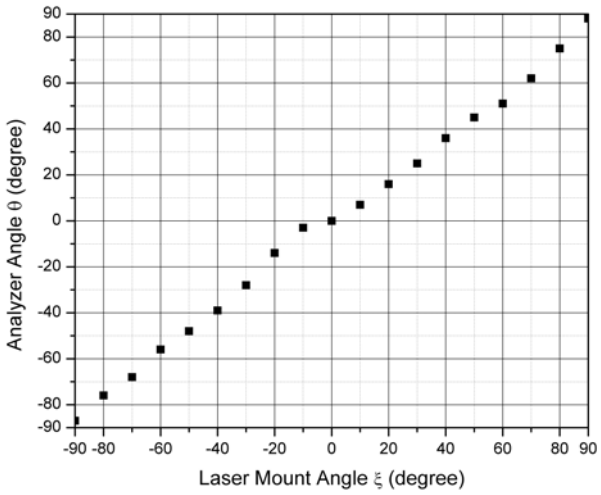

Fig. 6G Rotation angle θ of the analyzer, plotted as a function of the rotation angle ξ of the laser.

By rotating the laser mount, the light can be polarized horizontally (in-plane with the microsphere equator) or perpendicularly (normal to the equator plane). The in-plane light will excite the TM resonances, whereas preferential TE mode excitation will be possible with the perpendicular polarization.

As shown in Fig. 6H, the laser was rotated from ξ = 0º to 90º while holding the microsphere in contact with the etched section of the fiber, and the changes in the resonance spectrum were observed.

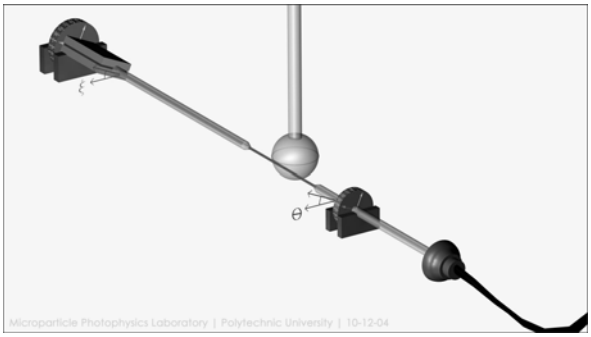

Fig. 6H The laser rotation setup with a microsphere. The analyzer is used to check the polarization direction, but taken out for shift measurements and spectrum recordings. Note that the microsphere contacts the etched fiber at the sphere's equator (i.e., the largest radius) to ensure that the light orbit is in the equatorial plane.

The existing resonance dips disappear gradually as the angle ξ increases and new dips appear when ξ reaches 90º. The change is reproducible and reversible. Fig. 6I shows the spectra recorded at ξ = 0º and 90º. The resonance dips at ξ = 0º are assumed to be those of TM modes and the dips at ξ = 90º TE modes. The dip patterns are similar in two spectra except that the resonance dips appear at different wavelengths. The spacing between the nearest pair of TM dip and TE dip is ~0.003nm (calculated for prominent dips). Fig. 6I shows a typical example.

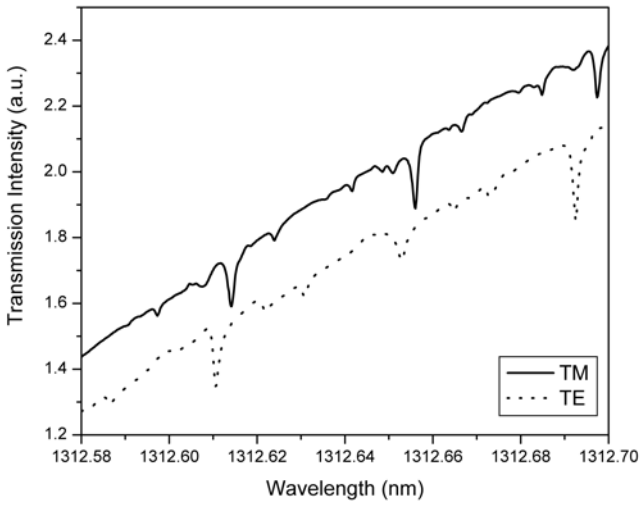

Fig. 6I Resonance spectra at ξ = 0º (solid line) and 90º (dotted line).

The results obtained in the laser rotation clearly demonstrate the excitation of different modes in the microsphere. Resonance shift measurements in two orthogonal polarization directions will verify the assignment of polarizations. We will carry out experiments for adding NaCl to the surrounding solution and compare the shift with our theory, Eqn. 6.3 and 6.4.

6.4 NaCl Experiments

Addition of NaCl to the sample cell will increase the solution refractive index homogeneously. We have treated the refractive index change in the medium as an infinitely thick layer in Chapter 4. Ions near a charged surface form a diffuse electrical double layer.[58] The Debye length, $1/\kappa$, characterizes the thickness of this diffuse layer. At 25ºC, the Debye length in nm is given by $1/\kappa = 0.304[\mathrm{NaCl}]^{-1/2}$, where [NaCl] is the salt concentration in mol/L. At [NaCl]=0.1 M, $1/\kappa$ is 0.96 nm. The diffuse layer is sufficiently thin, so that the ion concentration in the solution can be considered uniform throughout the accessible volume including right next to the microsphere surface in our experiments.

The dn/dc value of NaCl is 0.17010 ml/g at 632.8 nm wavelength at 25ºC. Using Eqn 6.3 and 6.4, we can calculate the expected fractional wavelength shift for a given NaCl concentration increase. If TM mode resonances are excited by the horizontal light, the measured $\Delta\lambda/\lambda$ should agree with the theoretical TM $\Delta\lambda/\lambda$.

The experiments were carried out using the basic set up described in Chapter 3 with the pigtailed 1300 nm DFB laser as the light source and setting the laser angle to the horizontal (vertical) polarization for TM (TE) mode measurements. The extinction ratio was ~ 200 for all the experiments. The microspheres were cleaned with the strong acid and used without any further chemical modifications. The sample cell was filled with 900 µl PBS and the cell temperature was maintained at 25ºC. The solution was mixed with a magnetic stir bar. An NaCl stock solution (0.0631 g/ml) was added to the sample cell in 20 µl increments.

Fig. 6J compares the theoretical fractional wavelength shift for the TM theory and the measured shift in the horizontal polarization. Fig. 6K shows the theoretical shifts for the TE mode and the measurements with the vertical polarization. The resonance shifts of all the prominent dips are plotted from each experiment. The error in measurements due to uncertainties in reading the resonance dip positions is shown as the error bar in the graphs. TM and TE shifts were measured using the same microsphere in Experiment 1. Experiment 2 and 3 used different microspheres for TE and TM measurements.

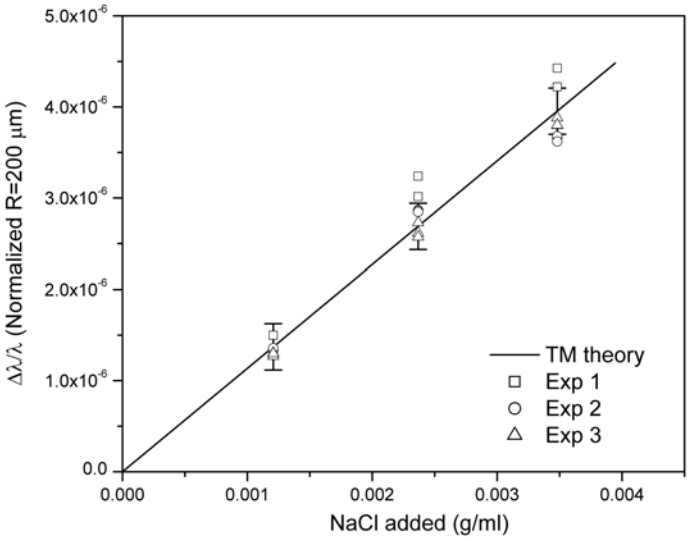

Fig. 6J The fractional resonance shifts due to NaCl addition: Measurements (symbols) and TM theory (line).

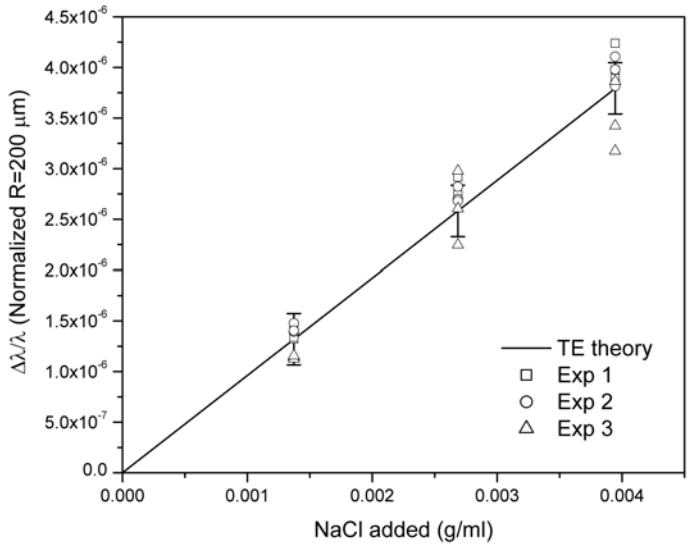

Fig. 6K The fractional resonance shifts due to NaCl addition: Measurements (symbols) and TE theory (line).

The experimental results agree well with the theory in each polarization and confirm our idea that the horizontally (vertically) polarized light preferentially stimulates TM (TE) resonance modes. It is important to note that not all dips shift by the same amount even though they are

in the same polarization (see for example, Exp 3 in Fig 6K). Although resonance dips are in the same polarization, the mode order ν can be different for each resonance mode. The mode order difference may account for the variations in the shift amount.

TM to TE resonance shift ratio for NaCl addition is 1.18, in agreement with the one predicted by Eqn. 6.3 and 6.4. TM and TE shift differences have never been studied using a silica microsphere. Polarization-specific mode excitation greatly enhances the WGM sensor's capability as a refractive index change detector.

Detection of refractive index change based on optical resonance shifts has been reported. A polymer microring with Q ~ 4000 was used to detect the refractive index change in the medium by increasing the glucose concentration.[59] The estimated sensitivity limit is 2.4×10^{-3} g/ml for glucose. Since the Q factor of our WGM sensor is 1000 times larger, the latter should perform 1000 times better. The smallest fractional shift we can detect is $\sim 10^{-8}$, which translates into the smallest detectable Δn_m of 10^{-7}.[11] The WGM sensor should be able to detect a $\sim 6 \times 10^{-6}$ g/ml NaCl concentration change.

Next we discuss the TM to TE shift ratio for α-lactalbumin layer formation.

6.5 α-Lactalbumin Experiments

α-Lactalbumin (LA) layer formation was carried out as described in Chapter 5. A LA stock solution was prepared in PBS at pH 7.4. 20 μl of the stock solution was added to the sample cell containing 980 μl PBS under constant mixing at 25ºC. The final LA concentration was 1μM. TM and TE modes were measured separately. Four microspheres used in these experiments were modified with amine by the solution method in the same batch in order to minimize the surface variation. Tables 4 and 5 summarize the shifts measured for prominent dips from TM and TE mode excitations.

Table 4. TM mode resonance shifts due to LA layer formation.

TM mode excitation	Exp 1 $(\Delta\lambda/\lambda)*R$ (nm)	Exp 2 $(\Delta\lambda/\lambda)*R$ (nm)	Exp 3 $(\Delta\lambda/\lambda)*R$ (nm)
Resonance Dip 1	1.713	1.776	1.723
Resonance Dip 2	1.693	1.702	1.688
Resonance Dip 3	1.550	-	-

Table 5. TE mode resonance shifts due to LA layer formation.

TE mode excitation	Exp 4 $(\Delta\lambda/\lambda)*R$ (nm)	Exp 5 $(\Delta\lambda/\lambda)*R$ (nm)	Exp 6 $(\Delta\lambda/\lambda)*R$ (nm)
Resonance Dip 1	1.738	1.730	1.735
Resonance Dip 2	1.867	1.618	1.705
Resonance Dip 3	1.737	-	1.689

The average of $(\Delta\lambda/\lambda)*R$ for the TM mode is 1.69 ± 0.07 nm. The average for the TE mode is 1.73 ± 0.07 nm. The TM to TE shift ratio is 0.98 ± 0.07. The experimental value is close to the ratio 1 expected for a layer of packed spheres of refractive index 1.5.

6.6 Ethylene Glycol Experiments

Ethylene glycol (EG, $C_2H_6O_2$, 62.07 g/mol) is a clear liquid at room temperature and its neat refractive index is 1.47. It belongs to C_{2h} point group (Fig. 6L).

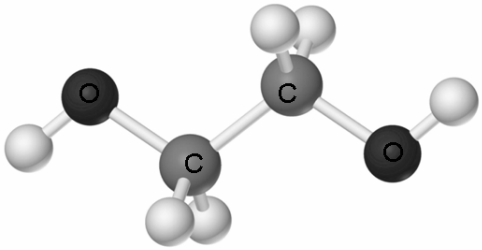

Fig. 6L Ethylene glycol structure, stick and ball model.

The interest in measuring the resonance shift due to EG addition was twofold. First, dn/dc value of EG is known (0.0993 g/g) [60] and therefore measured shifts can be compared with the theoretical values calculated from Eqn. 6.3 and 6.4. Second, the two OH groups in EG may form hydrogen bonds with surface silanol groups. It has been shown that, when the molecule is adsorbed onto the surface from the vapor phase, EG molecules form hydrogen bonds with surface silanols.[61] EG may adsorb onto the microsphere from aqueous phase. Then, the resonance shift will be the result of combined perturbations: surface adsorption and refractive index change in the medium. This combined effect has not been observed before. Since EG has nearly the same refractive index as silica, adsorbed EG will be just like adding silica to the surface.

EG addition experiments were carried out as follows. A 5 μl EG was added to the sample cell, containing 850 μl deionized water at 25ºC. For each polarization, the injection was repeated three times under constant mixing. A plot of the resonance shift against the concentration of EG in the surrounding solution is shown in Fig. 6M.

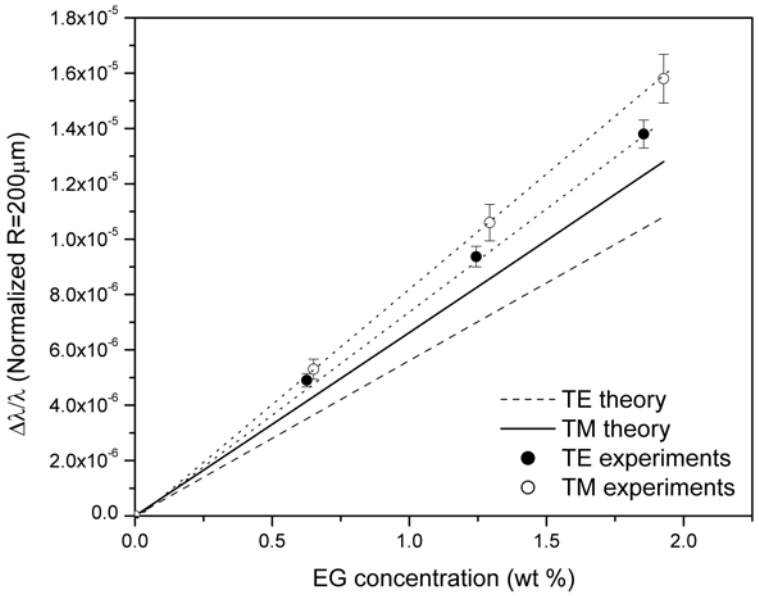

Fig. 6M Normalized fractional wavelength shifts against EG concentration. The expected shift from dn/dc is shown as a solid line (TM) and a dashed line (TE). The error bars indicate the spread of data for all prominent dips observed in two experiments.

The measured resonance shifts are greater than the expected shift based on the bulk refractive index change. The difference is approximately 1.14 x 10^{-6} and 9.96 x 10^{-7} for TE and TM mode respectively.

The extra shift is associated to EG adsorption onto the surface. The time trace of the resonance shift for EG adsorption does not follow a logarithmic growth pattern which was observed for protein and PLL adsorption (see Fig. 4E), but follows the pattern of NaCl addition (see Fig. 4F). The shift occurs immediately after EG injection.

Suppose that a measured shift is the sum of the two types of perturbations, then we can write

$$\frac{\Delta\lambda}{\lambda} = \left(\frac{\Delta\lambda}{\lambda}\right)_{\text{adsorption}} + \left(\frac{\Delta\lambda}{\lambda}\right)_{\text{dn/dc}}. \qquad (6.5)$$

$\left(\Delta\lambda/\lambda\right)_{\text{adsorption}}$ adds extra ~30% (taking the mean of TE and TM measurements) and is approximately 1x10^{-6} for each EG injection. We would like to estimate how many EG molecules are hydrogen-bonded to the surface. The α_{ex} in SI unit of EG molecule can be calculated from its dn/dc value and MW:

$$\frac{\alpha_{ex}}{4\pi\varepsilon_0} = \frac{n}{2\pi}\left(\frac{dn}{dc}\right)\frac{MW}{N_A}. \qquad (6.6)$$

α_{ex} is $(4\pi\varepsilon_0)$2.17x10^{-24} cm^3. $\left(\Delta\lambda/\lambda\right)_{\text{adsorption}}$ in terms of α_{ex} and protein number density σ_N is:[4]

$$\left(\frac{\Delta\lambda}{\lambda}\right)_{\text{adsorption}} = \frac{\alpha_{ex}\,\sigma_N}{\varepsilon_0\left(n_s^2 - n_m^2\right)R} \text{ (in SI)}. \qquad (6.7)$$

Together with R=200μm, we estimate the surface density of EG to be ~2.88x10^{14} cm^{-2}. The surface area of the sphere is 2.51x10^{-3} cm^2 for R=200μm. Thus, roughly 7.2x10^{11} EG molecules are adsorbed to the surface in one injection. 5μl EG injection delivers 5.5x10^{19} molecules to the sample cell. A tiny fraction of EG associates with the silica surface.

The higher TE value compared with TM suggests face-on adsorption of EG on the surface. If EG forms hydrogen bonds through its two OH groups, the molecule will lie flat on the surface. Because of two oxygen atoms, EG may have a greater polarizability in the direction parallel to the molecular axis connecting two OH groups than in the direction of C_2 axis.

The EG experiments indicate that a planer molecule adsorbed in the side-on orientation will result in a greater TM excess shift than the TE excess shift. The idea will be tested using phenol.

6.7 Phenol Molecules at Surface

Phenol has one OH group (Fig. 6N), which is known to form a hydrogen bond with surface silanols.[62]

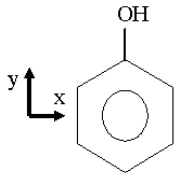

Fig. 6N Phenol molecule. Z-axis points out of the xy plane.

The ring orientation has been studied using biphenyl-4-ol on hydrogenated silicon wafer and benzenethiol on Gold(111) surface.[63,64] The tilt angle φ, defined as the angle between the surface normal and the aromatic ring backbone through the substituent (Fig. 6O) is approximately 23º~30º. The twist angle χ, which indicates the orientation of the ring face, is reported as 0º on Gold(111) and estimated 32º on the silicon surface.

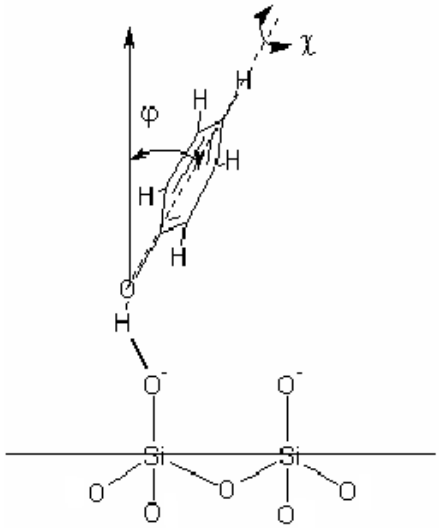

Fig.6O Expected phenol molecular orientation on silica surface. φ is the tilt angle and χ is the twist angle defined by the O-phenyl ring plane and the silica surface

plane. When $\chi = 0^{o}$, the phenol molecular x-axis is parallel to the surface. The thick line indicates a hydrogen bonding between the silanol and phenol.

Phenol has refractive index of 1.5425. The differential refractive index of phenol solution was measured using an Abbe refractometer in the concentration range up to 0.06 g/ml with the result of dn/dc being 0.1924ml/g at 589 nm.

The phenol experiments were conducted by injecting a 20 μl phenol stock solution (0.594 M) to 900 μl deionized water in the sample maintained at 25ºC under constant mixing. All microspheres were cleaned with acids to fully hydroxylate the silica surface. With TM modes excited, three injections were carried out. Then the sample cell was emptied and refilled with 900 μl deionized water. The microsphere was rinsed and reused for TE mode measurements. The DFB laser was rotated to excite TE modes and the injection was repeated three times. The injection caused the resonance shift immediately as in NaCl and EG experiments. Fig. 6P shows the results of three experiments.

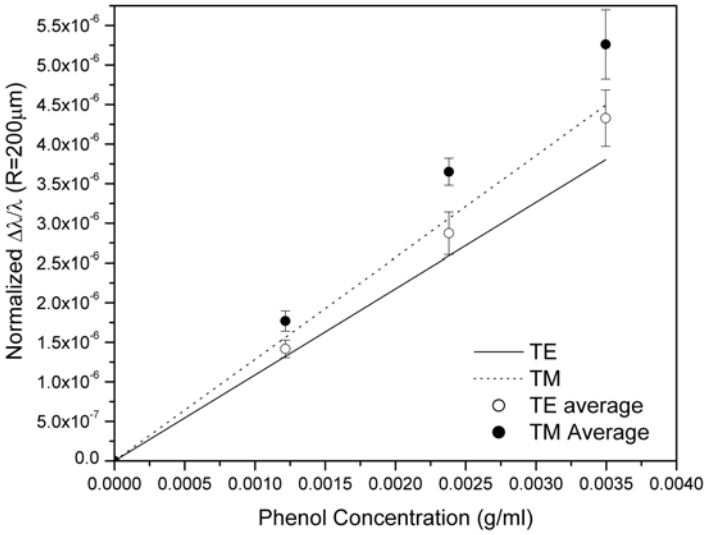

Fig. 6P Normalized fractional wavelength shift due to phenol addition. The average of three experiments is plotted for TM ( ) and TE ( ). Calculated dn/dc shifts based on Eqn. 6.3 and 6.4 are shown as a solid line (TM) and a dotted line (TE).

The measured shifts are higher than the shifts estimated for the bulk refractive index change. Each phenol injection added an excess shift $\Delta\lambda/\lambda \sim 1.75 \times 10^{-7}$ for TE (std 9%) and $\sim 2.57 \times 10^{-7}$ for TM (Std 8%). The excess shift is ascribed to adsorbed phenol molecules. Phenol shows a higher excess shift in the TM mode than it does in the TE mode. EG, on contrary, had the higher excess shift in TE mode.

The least squares linear fitting of the excess shift data gives the slope of 2.25×10^{-4} ml/g for TM and 1.36×10^{-4} ml/g for TE. The TM to TE ratio for the phenol adsorption is 1.65.

From the mean value of the TE and TM excess shifts, the phenol surface density can be estimated using Eqn. 6.7 and the isotropic mean value of the phenol polarizability tensor elements. The polarizability tensor elements are $\alpha_{xx} = 12.66$, $\alpha_{yy} = 11.41$, and $\alpha_{zz} = 4.45$ in units of $Å^3$ based on *ab initio* calculations.[65] The isotropic mean of the three diagonal components is 9.51 $Å^3$.

The estimated phenol density is 1.4×10^{14} cm^{-2}. The surface area of the sphere is 2.51×10^{-3} cm^2 for R=200 μm. Thus, roughly 3.5×10^{11} phenol molecules are adsorbed to the surface in one injection.

6.8 TE and TM Shifts and Molecular Orientation

In this section, we attempt to draw a quantitative picture of phenol orientation at the surface. In preceding sections, the anisotropy of the polarizability has been neglected, and the isotropic mean value of the polarizability tensor has been used in estimating the resonance frequency shift.

Polarizability of a molecule directly relates to resonance shifts. At the surface of the microsphere in resonance, interaction between a molecule and the applied field $\mathbf{E}_0$ induces the dipole moment $\delta\mathbf{p}$ in the molecule in excess of the displaced water. This reactive energy perturbs the mode energy and causes the shift in a resonant frequency.

$$\hbar\Delta\omega = -\frac{1}{2}\mathrm{Re}\left[\delta\mathbf{p}\cdot\mathbf{E}_0^*\right] \tag{6.8}$$

The dipole moment is the excess polarizability times the field:

$$\delta\mathbf{p} = \alpha_{ex}\,\mathbf{E}_0\,. \tag{6.9}$$

Therefore the shift in terms of the polarizability is

$$\hbar\Delta\omega = -\frac{1}{2}\left(\alpha_{ex}\left|\mathbf{E}_0\right|^2\right). \tag{6.10}$$

To investigate phenol orientation at the surface, we replace the isotropic mean of α_{ex} with the polarizability tensor elements.

We define three angles that are necessary to specify phenol orientation at the surface, as shown in Fig. 6Q.

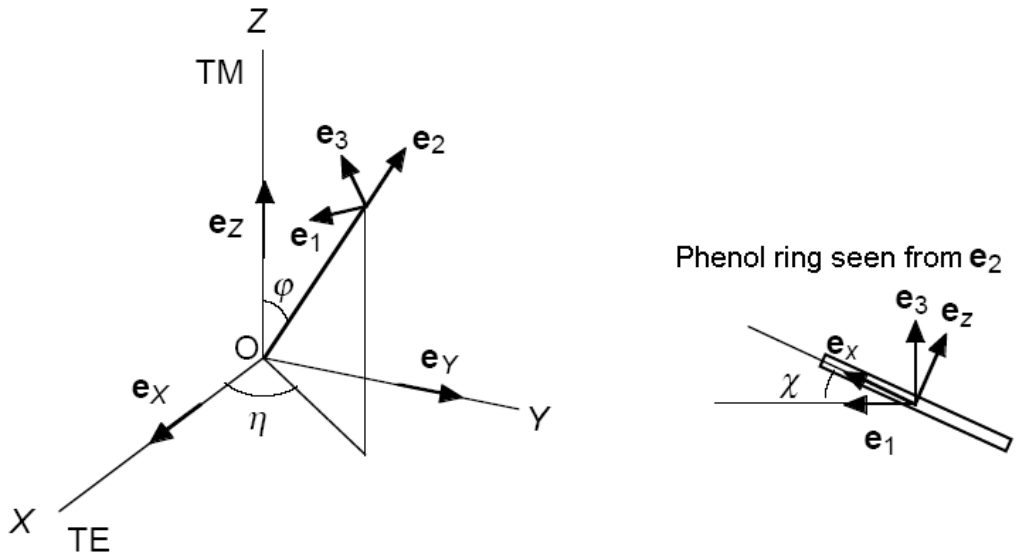

Fig. 6Q Three angles to define phenol orientation in the laboratory frame XYZ. Tilt angle φ, twist angle χ, and the azimuthal angle η. The phenol oxygen is placed at the origin. The unit vectors $\mathbf{e_1}$, $\mathbf{e_2}$, and $\mathbf{e_3}$ are introduced as a frame fixed on the phenol molecular axis. The molecular y-axis is in the direction of $\mathbf{e_2}$. $\mathbf{e_1}$ and $\mathbf{e_3}$ rotate together around $\mathbf{e_2}$.

Since TM is in Z direction and TE is in X direction, we find

$$\alpha_{ZZ} = \sin^2\varphi\sin^2\chi\,\alpha_{xx} + \cos^2\varphi\,\alpha_{yy} + \sin^2\varphi\cos^2\chi\,\alpha_{zz} \tag{6.11a}$$

$$\alpha_{XX} = \frac{1}{2}\alpha_{xx}(\cos^2\chi + \cos^2\varphi\sin^2\chi) + \frac{1}{2}\alpha_{yy}\sin^2\varphi + \frac{1}{2}\alpha_{zz}(\sin^2\chi + \cos^2\varphi\cos^2\chi). \tag{6.11b}$$

The phenol ring can freely rotate around the surface normal (i.e., the precession motion). Therefore, the azimuthal angle η should be averaged over all possible angles. The mean

square value of cos η or sin η is 1/2 in Eqn. 6.11b. The precession motion affects α_{XX}, not α_{ZZ}.

The angle φ and χ may vary between 0º and 90º. α_{XX} and α_{ZZ} change with φ and χ (Fig. 6R). The plots show the symmetric change in polarizability.

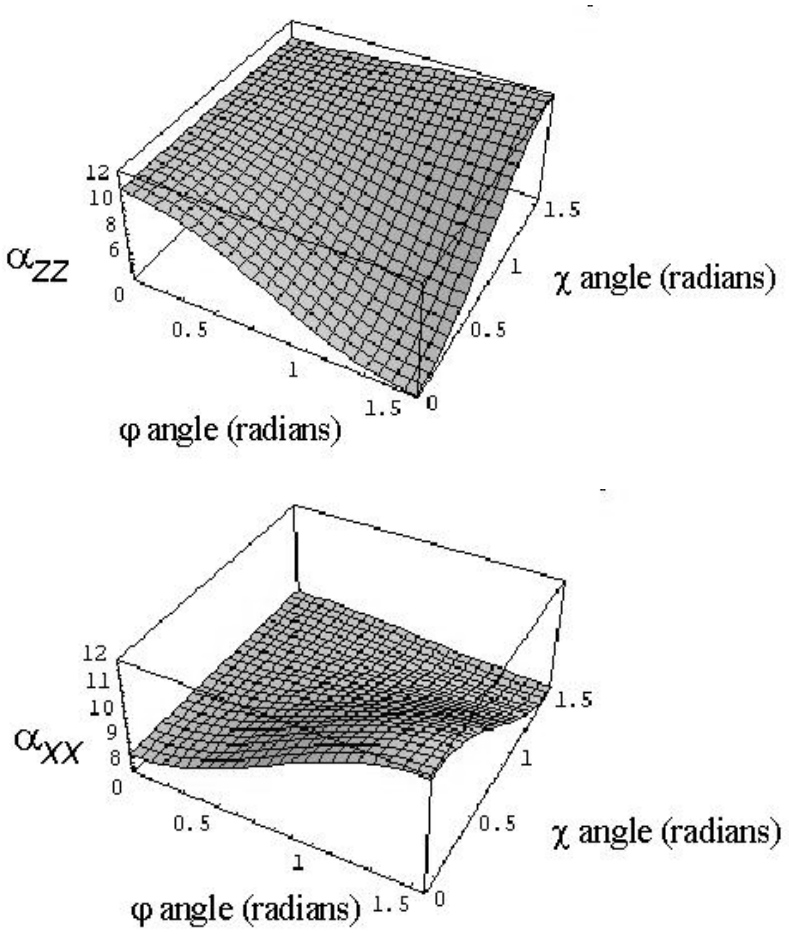

Fig.6R α_{ZZ} and α_{XX} as a function of φ and χ angles (in radians). The unit is $Å^3$.

A TM to TE ratio of the fractional wavelength shift can be expressed as:[4]

$$\frac{(\Delta\lambda/\lambda)_{TM}}{(\Delta\lambda/\lambda)_{TE}} = \frac{\alpha_{ZZ}\left|E_{TM}\right|^2/\left|E_{in}\right|^2}{\alpha_{XX}\left|E_{TE}\right|^2/\left|E_{in}\right|^2} \approx \frac{\alpha_{ZZ}\left|E_{TM}\right|^2}{\alpha_{XX}\left|E_{TE}\right|^2}. \qquad (6.12)$$

The electric field of a TM mode has normal (Z) and tangential (X) components. The intensity ratio of the two components is approximately $|E_X|^2/|E_Z|^2 \approx 0.145$. Since the tangential component of the TM mode also interacts with phenol, Eqn. 6.12 should be rewritten as

$$\frac{(\Delta\lambda/\lambda)_{TM}}{(\Delta\lambda/\lambda)_{TE}} \approx \frac{(0.873\alpha_{ZZ} + 0.127\alpha_{XX})|E_{TM}|^2}{\alpha_{XX}|E_{TE}|^2}. \qquad (6.13)$$

From Eqn. 6.13, we find the ratio of α_{ZZ} to α_{XX}:

$$\frac{\alpha_{ZZ}}{\alpha_{XX}} \approx \frac{1}{0.873}\left[\frac{(\Delta\lambda/\lambda)_{TM}/(\Delta\lambda/\lambda)_{TE}}{|E_{TM}|^2/|E_{TE}|^2} - 0.127\right]. \qquad (6.14)$$

The TM to TE ratio for the excess shifts is 1.65 from our experiment. With the estimated field intensity ratio as $|E_{TM}^2|/|E_{TE}^2| \approx (n_s/n_m)^4 = 1.49$, α_{ZZ}/α_{XX} is 1.12. Using Eqn. 6.11a and 6.11b, we evaluate the angles for α_{ZZ}/α_{XX} is 1.12. Given the standard deviation of 9% (taking the higher TE value), we estimate $\varphi = 27^\circ \pm 3^\circ$ and $\chi = 29^\circ \pm 4^\circ$.

The tilt angle from our measurement is similar to the reported values.[63,64] The twist angles are reported as 0º on gold and estimated 32º on hydrogenated silicon,[63,64] and our value is close to 32º.

6.9 Conclusion

We have demonstrated polarization-specific excitation of WGMs in a silica microsphere and measured TM and TE shift differences. To our knowledge, this is the first experiment to report TM and TE resonance shifts for protein layer formation and homogeneous refractive index change in the surrounding medium.

We also investigated the molecular orientation of phenol at the fully hydroxylated silica surface. Based on the excess shift measured at the two polarizations, we find the tilt and twist angles of the phenyl ring to be 27º±3º and 29º±4º, similar to the angles reported in the literature. The WGM sensor can measure anisotropic interactions between a molecule and the field.

Having confirmed the polarization-specific excitation of resonances, we can improve the WGM sensor setup. Using two lasers, one set for TM excitation and the other for TE

excitation, and multiplexing the two lights using an evanescent coupler as we have demonstrated in Chapter 4 will allow us to measure simultaneously TE and TM shifts in one microsphere.

Chapter 7

The Future of a Whispering Gallery Mode Sensor

The future generation of the WGM sensor will be miniaturized, and a microfluidic cell will be implemented. The optics and the electronics can be made smaller and integrated on a chip. Many microspheres can be multiplexed with one optical fiber (or waveguide) for parallel detection. The surface variations will provide specificity for multiple sample detection. Multi-wavelengths and dual polarization measurements will enable detailed analyses of detected molecules. We envision a powerful, high throughput-sensing devise based on the resonance frequency shift of the WGM.

Specially, a flow cell will open up a new opportunity for the WGM sensor in pharmaceutical industry. The flow cell will enable us to measure adsorption and desorption of analyte-ligand interactions. Kinetic data can be analyzed to determine the rate constant for the adsorption, k_a, and the desorption, k_d, based on a model of the interaction. It will be interesting to study a drug molecule binding to a target protein with or without a competitive binding. The WGM will be used to screen candidate drug molecules for the optimum binding.

With wide variations of the WGM sensor applications in our sight, we emphasize the importance of theory. Considering that our experiments are carried out on spheroids with eccentricities ~0.05, and that theory at present utilizes spherical photon states, it is surprising that the theory and experiments agree so well. In the future as perturbations are stronger (i.e. larger a/R, n_p/n_s) one will probably have to re-think the theory. However it is clear from Fig.5I that over a large range of protein sizes the sphere approximation describes the experimental results within the usual experimental uncertainties.

References

1. K. Vahala, "Optical Microcavities," Nature, **424**, 839 (2003).
2. F. Vollmer, D. Braun, A. Libchaber, M. Khoshsima, I. Teraoka, and S. Arnold, "Protein Detection by Optical Shift of a Resonant Microcavity," Appl. Phys. Lett., **80**, 4057 (2002).
3. F. Vollmer, S. Arnold, D. Braun, I. Teraoka, and A. Libchaber, "Multiplexed DNA Quantification by Spectroscopic Shift of Two Microsphere Cavities," Biophys. J., **85**, 1974 (2004).
4. S. Arnold, M. Khoshsima, I. Teraoka, S. Holler, and F. Vollmer, "Shift of Whispering-gallery Modes in Microspheres by Protein adsorption," Opt. Lett., **28**, 272 (2003).
5. D.S Weiss, V. Sandoghdar, J. Hare, V. Lefevre-Sequin, J.M. Raimond, and S. Haroche, "Splitting of High Q Mie Modes Induced by Light Backscattering in Silica Microsphere," Opt. Lett., **20** (1995).
6. A. Serpengüzel, S. Arnold, and G. Griffel, "Excitation of Resonances of Microspheres on an Optical Fiber," Opt. Lett., **20**, 654 (1995).
7. L. Reviakine, A.N. Morozov, and F.F. Rossetti, "Effects of Finite Crystal Size in the Quartz Crystal Microbalance with Dissipation Measurement System: Implications for data Analysis," J. Appl. Phys., **95**, 7712 (2004).
8. S. Arnold, M. Noto and F. Vollmer, "Consequences of extreme photon confinements in microcavities: I. Ultra-sensitive detection of perturbations by biomolecules," *Frontiers of optical spectroscopy: investigating extreme physical condition with advanced optical techniques*, Ed. by B. Di Bartolo (Kluwer Academic Publishers, Dordorecht, 2005), pp. 337-357.
9. G. Mie, "Beiträge zur Optik trüber Medien, speziell kolloidaler Metallösungen,"Ann. Phys. (Leipzig), **25**, 376 (1908).
10. L.M. Folan, "Characterization of the Accretion of Material by Microparticles using Resonant Ellipsometry," Appl. Optics, **31**, 2066 (1992).
11. I. Teraoka, S. Arnold, and F. Vollmer, "Perturbation Approach to Resonance Shifts of

Whispering-gallery Modes in a Dielectric Microsphere as a Probe to the Surrounding," J. Opt. Soc. Am. B, **20**, 1937 (2003).

12. D.Q. Chowdhury, S.C. Hill, and M.M. Mazumder, "Quality Factors and effective-average Modal gain or Loss in inhomogeneous Spherical Resonators-Application to 2-Photon Absorption," IEE. J. Quantum Electron., **29**, 2553 (1993).
13. M. Khoshsima, *Perturbation of Whispering Gallery Modes in Microspheres by Protein Adsorption: Theory and Experiment*, PhD thesis, Polytechnic University, Jan. 2004.
14. NFL Laser Diode NLK1B5E1AA Information Sheet, NEL America Inc., January (2002).
15. J.P. Laine, B.E. Little, and H.A. Haus, "Etch-eroded Fiber Coupler for Whispering-gallery Mode Excitation in High-Q Silica Microsphere," IEEE Photonics Technol. Lett., **11**, 1429(1999).
16. M.J. Heller, "DNA Microarray Technology: Devices, systems, and applications," Annual Review of Biomedical Engineering, **4**, 129 (2002).
17. Y. Lee, E.K. Lee, Y.W. Cho, T. Matsui, T. Kim, and M.H. Han, "Protein Chip: A highly sensitive protein microarray prepared by a novel method of protein immobilization for application of protein-protein interaction studies," Proteomics, **3**, 2289 (2003).
18. C.E. Jordan, B.L. Frey, S. Kornguth, and R.M. Corn, "Characterization of Poly-L-lysine Adsorption onto Alkanethiol-Modified Gold Surfaces with Polarization-Modulation Fourier Transformation Infrared Spectroscopy and Surface Plasom Resonance Measurements," Langmuir, 10, 3642 (1994).
19. H. Arwin, "Ellipsometry on Thin Organic Layers of Biological Interest: Characterization and Applications," Thin Solid Film, **377/378**, 48 (2000).
20. C.C. Lam, P.T. Leung and K. Young, "Explicit Asymptotic Formula for the Positions, Width, and Strength of Resonances in Mie Scattering," J. Opt. Soc. Am. B, **9**, 1585 (1992).
21. International Critical Tables of Numerical Data, Physics, Chemistry and technology 1st Electronic edition, Volume VII.

22. I.H. Malitson, “Interspecimen Comparison of the Refractive Index of Fused Silica,” J. Opt. Soc. Am. B., **55**, 1205 (1965).
23. T.J. Su, J. R. Lu, R.K. Thomas, Z.F. Cui, and J. Penfold, “The Conformational Structure of Bovine Serum Albumin Layers Adsorbed at the Silica-water Interface,” J. Phys. Chem. B., **102**, 8100 (1998).
24. T.J. Su, J. R. Lu, R.K. Thomas, and Z.F. Cui, “Effect of pH on the Adsorption of Bovine Serum Albumin at the Silica/water Interface Studied by Neutron Reflection,” J. Phys. Chem. B., **103**, 3727 (1999).
25. P.M. Claesson, E. Blomberg, J.C. Fröberg, T, Nylander, and T. Arnebrant, “Protein Interactions at Solid Surfaces,” Adv. Colloid Interface. Sci., **57**, 161 (1991).
26. M.A. Cohen Stuart, G.J. Fleer, J. Lyklema, W. Norde, and J.M.H.M. Scheutjens, “Adsorption of Ions, Polyelectrolytes, and Proteins, Adv. Colloid Interface. Sci., **34**, 477 (1991).
27. C. Haynes, and W. Norde, “Structures and Stabilities of Adsorbed Proteins,” J. Colloid Interface Sci., **169**, 313 (1995).
28. W. Norde, “Adsorption of Proteins from Solution at the Solid-liquid Interface,” Adv, Colloid Interface, Sci., **25**, 267 (1986).
29. K. Kikuchi, and H. Akutsu, “Hydrodynamic Behavior and Molecular-conformation of Poly(L-lysine HBr) in Carbonate Buffer Solution,” Biopolymers, **20**, 345 (1981).
30. A. Subramanian, S.J. Kennel, P.I. Oden, K.B. Jacobson, J. Woodward, and M.J. Doktycz, “Comparison of Techniques for Enzyme Immobilization on Silicon Supports,” Enzymes and Microbial technology, **24**, 26 (1999).
31. M. Muthukumar, “Adsorption of a Polyelectrolyte Chain to a Charged Surface,” J. Chem. Phys., **86**, 7230 (1987).
32. C. Picart, Ph. Lavalle, P. Hubert, F.J.G. Cuisinier, G. Decher, P. Schaaf, and J.C. Voegel, “Buildup Mechanism for Poly(L-lysine)/Hyaluronic Acid Films onto a Solid Surface,” Langmuir, **17**, 7414 (2001).
33. M. Biesalski, D. Johannsmann, and J. Ruhe, “Natural and Charged Polymer Brushes at Solid Surface,” Macromolecular Symposia, **145**, 113 (1999).

34. P.F. Luckham, and J. Klein, "Forces Between Mica Surfaces Bearing Adsorbed Poly-electrolyte, Poly-L-lysine, in Aqueous-media," J. Chem. Soc., Faraday Trans. 1, **80**, 865 (1984).

35. E. Pennisi, "A Low Number Wins the GeneSweep Pool," Science, **300**, 1484 (2003).

36. D. Eisenberg and D. Crothers, *Physcial Chemistry with Applications to the Life Science* (The Benjamin/Cummings Publishing Company, INC., California, 1979), p.219.

37. I.N. Levine, *Physical Chemistry*, 4th Ed., (McGrew-Hill, INC., New York, 1995), p.366.

38. B.J. Yoon and A.M. Lenhoff, "Computation of the Electrostatic Interaction Energy between a Protein and a Charged Surface," J. Phys. Chem., **96**, 3130 (1992).

39. R. Kurrat, J.E. Prenosil, and J.J. Ramsden, "Kinetics of Human and Bovine Serum Albumin Adsorption at Silica-titania Surfaces," J. Colloid Interface Sci., **185**, 1 (1997).

40. S.A. Sukhishvili and S. Granick, "Adsorption of Human Serum Albumin: Dependence on Molecular Architecture of the Oppositely Charged Surface," J. Chem. Phys., **110**, 10153 (1999).

41. W. Norde, and C.E. Giacomelli, "BSA Structural Changes during Homomolecular Exchange between the Adsorbed and the Dissolved States," J. Biotech., **79**, 259 (2000).

42. H.E. Bergna, "Colloid Chemistry of Silica," *The Colloid Chemistry of Silica*, H.E. Bergna, Ed., American Chemical Society, Washington, DC 1994, pp1- 47.

43. K. Albert and E. Bayer, "Characterization of Bonded Phases by Solid-state NMR Spectroscopy," J. Chromatogr. **544**, 345 (1991).

44. T. Hiemstra, J.C.M. de Wit, and W.H. van Riemsdijik, "Multisite Proton Adsorption Modeling at the Solid/solution Interface of (Hydr)oxides: A New Approach," J. Colloid Interface Sci., **133**, 105 (1989).

45. P. Schindler and H.R. "Die Acitat von Silanolgruppen," Kamber, Helv. Chim. Acta, **51**, 1781 (1968).

46. M.L. Hair and W. Hertl, "Acidity of Surface Hydroxyl groups," J. Phys. Chem., **74**, 91 (1970).

47. G.H. Bolt, "Determination of the Charge Density of Silica Soils," J. Phys. Chem., **61**, 1166 (1957).

48. E.D. Chrysina, K. Brew, and K.R. Acharya, "Crystal Structures of Apo- and Holo-bovine α-Lactalbumin at 2.2-Å Resolution Reveal an Effect of calcium on Inter-lobe Interactions," J. Biol. Chem., **275**, 37021 (200).

49. A.P. Minton, "Adsorption of Globular Proteins on Locally Planar Surfaces. II. Models for the Effect of Multiple Adsorbate Conformations on Adsorption Equilibria and Kinetics," Biophys. J., **76**, 176 (1999).

50. C.R. Cantor and P.R. Schimmel, *Biophysical Chemistry Part II*, W.H. Freeman and Company, New York, 1980, p554.

51. P.A. Cuypers, W.TH. Hermens, and H.C. Hemker, "Ellipsometry as a Tool to Study Protein Films at Liquid-solid Interfaces," Biochemistry, **84**, 56-67 (1978).

52. B. Liedberg, B. Iversson, I. Lundström, and W.R. Salaneck, "Fourier Transform Infrared Reflection Adsorption Spectroscopy (FT-IRAS) of Some Biologically Important Molecules," Prog. Colloid. Polym. Sci.,**70**, 67-75 (1985).

53. S. Torquato, "Mean Nearest-Neighbor Distance in Random Packing of Hard D-Dimensional Spheres," Phys. Rev. Lett., **74**, 2156 (1995).

54. X.M. He, and D.C. Carter, "Atomic Structure and Chemistry of Human Serum Albumin," Nature, **358**, 209 (1992).

55. S.H. Armstrong Jr., M.J.E. Budka, K.C. Morrison, and M. Hasson, "Preparation and Properties of Serum and plasma Proteins," J. Am. Chem. Soc., **69**, 1747 (1947).

56 F. Vollmer, "Resonant Detection of Nano to Microscopic Objects Using Whispering Gallery Modes," Thesis. Rockefeller University (2004).

57. I. Teraoka and S. Arnold, to be submitted.

58. J.N. Israelachvili, *Intermolecular and Surface Forces*, Academic Press, INC., San Diego, CA, 1988, p180.

59. C.Y. Chao and L.J. Guo, "Biochemical Sensors Based on Polymer Microrings with Sharp Asymmetrical Resonance," Appl. Phys. Lett., **83**, 1527 (2003).

60. S. Dai, S.T. Sio, K.C. Tam, and R.D. Jenkins, "Rheology and Aggregation Behavior of Hydrophobically Modified Urethane Ethoxylate in Ethylene Glycol – Water Mixture," Macromolecules, **36**, 6260 (2003).

61. D. Liu, G. Ma, M. Xu, and H.G. Allen, "Adsorption of Ethylene Glycol Vapor on α-Al_2O_3 (0001) and Amorphous SiO_2 Surfaces: Observation and Surface Hydroxyl Groups as Sorption Sites," Environ. Sci. Technol., **39**, 206 (2005).

62. P. Voumard, Q. Zhan, and R. Zenobi, "Adsorption of Monosubstituted Benzenes on Low Surface Area Silica Studied by Temperature-Programmed Desorption and Laser-Induced Thermal Desorption Methods," Langmuir, **11**, 842 (1995).

63. M. Zharnikov, A. Küller, A. Shaporenko, E. Schmidt, and W. Eck, "Aromatic Self-Assembled monolayers on Hydrogenated Silicon," Langmuir, **19**, 4682 (2003).

64. L.J. Wan, M. Terashima, H. Noda, and M. Osawa, "Molecular Orientation and Ordered Structure of Benzenethiol Adsorbed on Gold(111), J. Phys. Chem. B., **104**, 3563 (2000).

65. R. Chelli and P. Procacci, "A Transferable Polarizable Electrostatic Force field for Molecular Mechanics Based on the Chemical Potential Equalization Principle," J. Chem. Phys., **117**, 9175 (2002).

Appendix 1 Laplace Transform

In Chapter 4.4, we introduced the excess dielectric profile $\kappa_e(r-R)$ and the general form of fractional wavelength shift, Eqn. 4.9:

$$\frac{\Delta\lambda}{\lambda} = \frac{1}{R(n_s^2 - n_m^2)} \int_R^\infty \kappa_e(r-R)\, e^{-(r-R)/L} dr. \qquad (A1)$$

For the nanolayer characterization, we assumed that $\kappa_e = n_\ell^2 - n_m^2$ where n_ℓ and n_m are the refractive indices of the layer and the medium respectively. n_ℓ extends from the microsphere surface to the layer thickness t. κ_e can be considered a step function (Fig. 1).

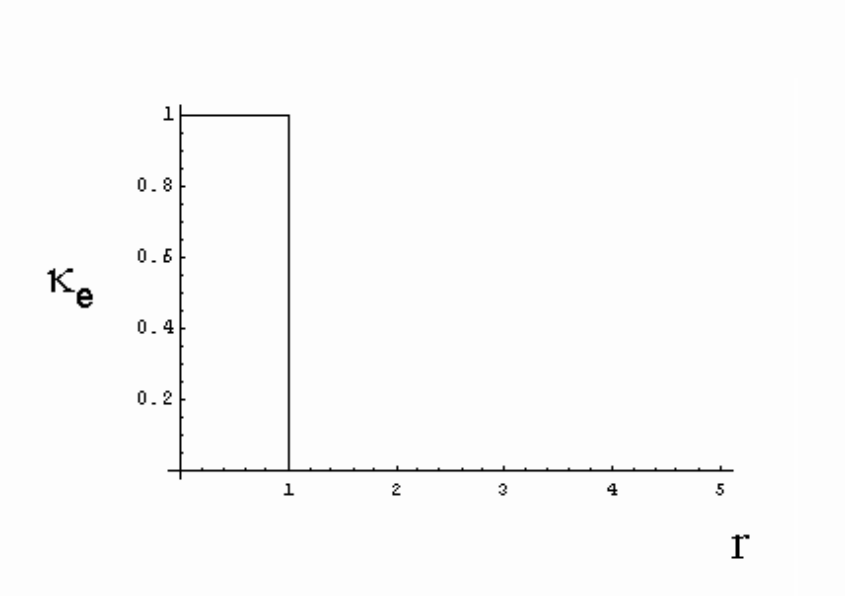

Fig. 1 Normalized κ_e profile for a layer. r =0 set at the sphere surface.

The Laplace transform X(m) is defined for x(n)as

$$X(m) = \int_0^\infty x(n)\exp(-mn)\,dn. \qquad (A2)$$

For a unit step function x(n), X(m) is 1/m. Our κ_e takes the form of x(n)-x(n-1). The transform of the normalized $\kappa_e(n)$ is

$$X(m) = \frac{1}{m} - \frac{e^{-m}}{m}. \qquad (A3)$$

Using Eqn. A3 as a model function, we can fit the form of the ratio S in Eqn. 4.13 (see Fig. 4B). The fit provides $X(m) = 0.578 + 0.425\exp(-m/188)$, which is $S \approx (L_1 / L_2) + (1 - L_1 / L_2)\exp(-t/190)$.

Consequently, if we obtain X(m) by having more than two data (i.e., measuring $\Delta\lambda/\lambda$ using more than two wavelengths, we find κ_e (r-R) by taking the inverse Laplace transform.

$$x(n) = \frac{1}{2\pi i}\int_{c-\infty}^{c+\infty} X(m)\exp(mn)\,dm \qquad \text{(A4)}$$

We can test our idea by selecting a different form for x(n). For example, $x(n) = \exp(-n)$, the excess dielectric profile takes the shape as shown in Fig. 2.

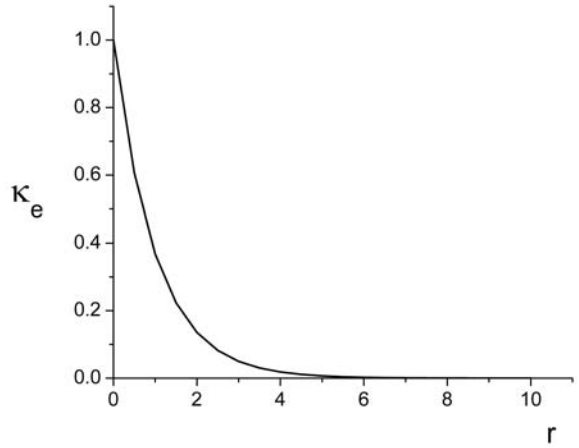

Fig.2 An example of a normalized κ_e, the function is $x(n) = \exp(-n)$.

The Laplace transform X(m) is

$$X(m) = \frac{1}{1+m}. \qquad \text{(A5)}$$

This function X(m) is what we expect to measure S as a function of thickness t.

Appendix 2 Surface Modification methods

All silane agents were purchased from Gelest Inc. Other chemicals are ACS reagent grade unless otherwise mentioned and purchased from Sigma-Aldrich (SA), Fisher Scientific (F), or Acros Organics (AO).

Silica Microsphere Cleaning

Preceding the modifications described below, a silica microsphere needs to be cleaned and dried. The acid cleaning using a piranha solution generates free silanol groups on the silica surface, making them available for subsequent chemical reactions. Drying will eliminate water molecules on the surface.

The piranha solution is a mixture of 30:70 volume mixture of hydrogen peroxide (H325-500, F) and concentrated sulfuric acid (A300-500, F). The solution should be made fresh because the oxidizing power of hydrogen peroxide weakens when exposed to air for a long time. The solution becomes very hot upon mixing. Handle very carefully.

Silica microspheres are immersed in the piranha solution for at least 10 minutes and rinsed with a copious mount of deionized water. The microspheres are then dried in the oven at 110ºC for 20 minutes.

Amine Surface

3-aminopropyltrimethoxysilane (SIA 0611.0) is mixed with alcohol (ethanol or methanol) to make up a 30% solution. A microsphere is immersed in the solution for 30 minutes and rinsed with ethanol. The microsphere is cured in the oven at 110ºC for 30 minutes.

Comments:

- The amine surface is not stable in the air. Modified microspheres cannot be stored.

- The choice of alcohol (either ethanol or methanol) did not change the result of amine modification. Ethanol is less toxic. Ethanol is recommend.
- Amine modification is often carried out with 2~3% silane solution using 95% ethanol (5% water and pH adjusted to 5.5) as the solvent. This method turned out to be very difficult for our microspheres. After the reaction, microspheres often failed to resonate.

Carboxyl Surface

An amine microsphere is further modified with succinic anhydride. Succinic anhydride (21956, AO) is recrystallized from N,N-dimethylformamide (DMF) /ether mixture. 0.1M succinic anhydride in DMF is prepared fresh, and the microsphere is immersed in this solution for 15 minutes. After rinsing with DMF, the microsphere is dried at 65ºC.

Methyl Surface

Chlorotrimethylsilane (11012, AO) is added to toluene to make up 30% (v/v) solution. A microsphere is immersed in the solution for 30 minutes and rinsed with toluene. The microsphere is dried in the oven at 110ºC.

PLL Surface

PLL solution (P8920, 0.1% w/v in water, MW 150,000 to 300,000 g/mol, SA) is diluted by factor of 10. A 4µl of the diluted PLL solution is transferred to a microsphere by a pipette, so that a droplet is hanging on the microsphere. The droplet should cover the entire microsphere surface. The microsphere is incubated until dry. When ready to use the microsphere, the sphere should be dipped in deionized water to remove the excess PLL.

Dextran Surface

Dextran (SO) is dissolved in deionized water at 10 mg/ml and a 4μl droplet is applied to a microsphere as in PLL coating. The microsphere is rinsed in deionized water before using.

Appendix 3 Resonance Mode Number ℓ

The mode number ℓ can be estimated by considering the angular momentum of a photon in a microsphere of n_s.

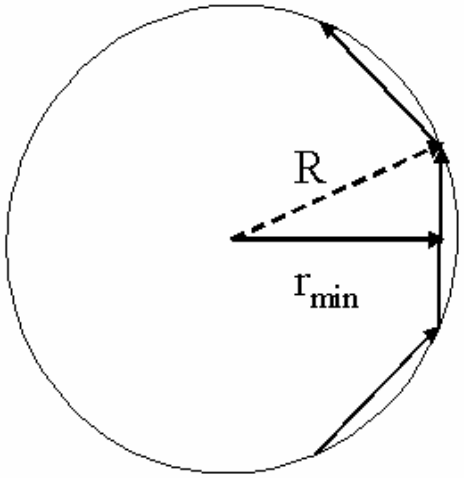

Fig. 3 Photon circumnavigating the circumference of a microsphere

We estimate the mode number using

$$\text{Angular momentum} = r_{min} \times \mathbf{p} = r_{min}(\hbar n_s k_0) \approx \hbar\sqrt{\ell(\ell+1)}, \qquad \text{(A6)}$$

And setting $r_{min} = R$,

$$n_s k_0 R \approx \sqrt{\ell(\ell+1)} \approx \ell + \tfrac{1}{2}. \qquad \text{(A7)}$$

For $n_s = 1.47$, R= 200 μm and $k_0 = 2\pi/1.3 = 4.83\ \mu m^{-1}$, ℓ is approximately 1420.

Appendix 4 Uniform Refractive Index Change in the Surrounding Medium and the Resonance Shift

To derive an analytical expression for the fractional wavelength shift for a uniform refractive index, Δn_m, in the surrounding medium, we go back to Eqn. 4.9 in Chapter 4.4.

$$\frac{\Delta\lambda}{\lambda} = \frac{1}{R(n_s^2 - n_m^2)} \int_R^\infty \kappa_e (r - R)\, e^{-(r-R)/L} dr \qquad \text{(A8)}$$

κ_e is the excess dielectric profile from the surface (r = R) and L is the wavelength dependent evanescent field length, $L = \left(2k_0\sqrt{n_s^2 - n_m^2}\right)^{-1}$.

κ_e can be expressed as $\delta\left(n_m^2\right) \approx 2 n_m \Delta n_m$ and can be taken out of the integral because it dose not depend on r (i.e., the change is the same for all r). We find

$$\frac{\Delta\lambda}{\lambda} = \frac{n_m \Delta n_m}{R(n_s^2 - n_m^2)} \int_0^\infty e^{-\xi/L} d\xi \qquad \text{(A9)}$$

with the exchange of variables r to ξ = r-R. Evaluating the integral, we obtain

$$\frac{\Delta\lambda}{\lambda} = \frac{n_m \Delta n_m}{k_0 R(n_s^2 - n_m^2)^{3/2}} \qquad \text{(A10)}$$

for a TE mode.

[35]

[36] Ref for kinetics

[37] isotherm

[38] B.J. Yoon and A.M. Lenhoff, "Computation of the Electrostatic Interaction Energy between a Protein and a Charged Surface," J. Phys. Chem., **96**, 3130 (1992).

[39] R. Kurrat, J.E. Prenosil, and J.J. Ramsden, J. Colloid Interface Sci., **185**, 1 (1997).

[40] S.A. Sukhishvili and S. Granick, "Adsorption of Human Serum Albumin: Dependence on Molecular Architecture of the Oppositely Charged Surface," J. Chem. Phys., **110**, 10153 (1999).

[41] W. Norde, and C.E. Giacomelli, "BSA Structural Changes during Homomolecular Exchange between the Adsorbed and the Dissolved States," J. Biotech., **79**, 259 (2000).

[42] H.E. Bergna, "Colloid Chemistry of Silica," *The Colloid Chemistry of Silica*, H.E. Bergna, Ed., American Chemical Society, Washington, DC 1994, pp1-47.

[43] K. Albert and E. Bayer, "Characterization of Bonded Phases by Solid-state NMR Spectroscopy," J. Chromatogr. **544**, 345 (1991).

[44] T. Hiemstra, J.C.M. de Wit, and W.H. van Riemsdijk, "Multisite Proton Adsorption Modeling at the Solid/solution Interface of (Hydr)oxides: A New Approach," J. Colloid Interface Sci., **133**, 105 (1989).

[45] P. Schindler and H.R. Kamber, Helv. Chim. Acta, **51**, 1781 (1968).

[46] M.L. Hair and W. Hertl, J. Phys. Chem., **74**, 91 (1970).

[47] G.H. Bolt, J. Phys. Chem., **61**, 1166 (1957).

[48] Alpha-lac crystal

[49] minton

[50] C.R. Cantor and P.R. Schimmel, *Biophysical Chemistry Part II*, W.H. Freeman and Company, New York, 1980 p554.

[51] P.A. Cuypers, W.TH. Hermens, and H.C. Hemker, "Ellipsometry as a Tool to Study Protein Films at Liquid-solid Interfaces," **84**, 56-67 (1978).

[52] B. Liedberg, B. Iversson, I. Lundström, and W.R. Salaneck, "Fourier Transform Infrared Reflection Adsorption Spectroscopy (FT-IRAS) of Some Biologically Important Molecules," **70**, 67-75 (1985).

[53] torquato

[54] BSA shape

[55] S.H. Armstrong Jr., M.J.E. Budka, K.C. Morrison, and M. Hasson, J. Am. Chem. Soc., **69**, 1747 (1947).

[56] F. Vollmer, "Resonant Detection of Nano to Microscopic Objects Using Whispering Gallery Modes," Thesis. Rockefeller University (2004).

[57] I. Teraoka and S. Arnold, to be submitted.

[58] jacob

[59] C.Y. Chao and L.J. Guo, "Biochemical Sensors Based on Polymer Microrings with Sharp Asymmetrical Resonance," Appl. Phys. Lett., **83**, 1527 (2003).

[60] S. Dai, S.T. Sio, K.C. Tam, and R.D. Jenkins, "Rheology and Aggregation Behavior of Hydrophobically Modified Urethane Ethoxylate in Ethylene Glycol – Water Mixture," Macromolecules, **36**, 6260 (2003).

[61] D. Liu, G. Ma, M. Xu, and H.G. Allen, "Adsorption of Ethylene Glycol Vapor on α-

Al_2O_3 (0001) and Amorphous SiO_2 Surfaces: Observation and Surface Hydroxyl Groups as Sorption Sites," Environ. Sci. Technol., **39**, 206 (2005).

[62] P. Voumard, Q. Zhan, and R. Zenobi, "Adsorption of Monosubstituted Benzenes on Low Surface Area Silica Studied by Temperature-Programmed Desorption and Laser-Induced Thermal Desorption Methods," Langmuir, **11**, 842 (1995).

[63] M. Zharnikov, A. Küller, A. Shaporenko, E. Schmidt, and W. Eck, "Aromatic Self-Assembled monolayers on Hydrogenated Silicon," Langmuir, **19**, 4682 (2003).

[64] LJ. Wan, M. Terashima, H. Noda, and M. Osawa, "Molecular Orientation and Ordered Structure of Benzenethiol Adsorbed on Gold(111), J. Phys. Chem. B., **104**, 3563 (2000).

[65] R. Chelli and P. Procacci, "A Transferable Polarizable Electrostatic Force field for Molecular Mechanics Based on the Chemical Potential Equalization Principle," J. Chem. Phys., **117**, 9175 (2002).